



**HAL**  
open science

## **WALLABY pre-pilot survey: two dark clouds in the vicinity of NGC 1395**

O Wong, A Stevens, B-Q For, T Westmeier, M Dixon, S-H Oh, G Józsa, T Reynolds, K Lee-Waddell, J Román, et al.

► **To cite this version:**

O Wong, A Stevens, B-Q For, T Westmeier, M Dixon, et al.. WALLABY pre-pilot survey: two dark clouds in the vicinity of NGC 1395. *Monthly Notices of the Royal Astronomical Society*, 2021, 507 (2), pp.2905-2921. 10.1093/mnras/stab2262 . hal-03577980

**HAL Id: hal-03577980**

**<https://hal.science/hal-03577980>**

Submitted on 16 Aug 2022

**HAL** is a multi-disciplinary open access archive for the deposit and dissemination of scientific research documents, whether they are published or not. The documents may come from teaching and research institutions in France or abroad, or from public or private research centers.

L'archive ouverte pluridisciplinaire **HAL**, est destinée au dépôt et à la diffusion de documents scientifiques de niveau recherche, publiés ou non, émanant des établissements d'enseignement et de recherche français ou étrangers, des laboratoires publics ou privés.

# WALLABY pre-pilot survey: two dark clouds in the vicinity of NGC 1395

O. I. Wong<sup>1,2,3</sup>★, A. R. H. Stevens<sup>1,2,3</sup>★, B.-Q. For<sup>1,2,3</sup>★, T. Westmeier<sup>1,2,3</sup>, M. Dixon,<sup>4</sup> S.-H. Oh,<sup>5</sup> G. I. G. Józsa,<sup>6,7,8</sup> T. N. Reynolds<sup>1,2,3</sup>, K. Lee-Waddell<sup>1,2</sup>, J. Román,<sup>9,10,11</sup> L. Verdes-Montenegro,<sup>9</sup> H. M. Courtois,<sup>12</sup> D. Pomarède,<sup>13</sup> C. Murugesan,<sup>1,3,4</sup> M. T. Whiting,<sup>14</sup> K. Bekki,<sup>2</sup> F. Bigiel,<sup>8</sup> A. Bosma<sup>1,15</sup>, B. Catinella<sup>1,2,3</sup>, H. Dénes,<sup>16</sup> A. Elagali,<sup>2,17</sup> B. W. Holwerda<sup>1,18</sup>, P. Kamphuis,<sup>19</sup> V. A. Kilborn,<sup>3,4</sup> D. Kleiner<sup>1,20</sup>, B. S. Koribalski<sup>1,14,21</sup>, F. Lelli,<sup>22</sup> J. P. Madrid,<sup>23</sup> K. B. W. McQuinn,<sup>24</sup> A. Popping,<sup>2,25</sup> J. Rhee,<sup>2,3</sup> S. Roychowdhury,<sup>2,3</sup> T. C. Scott<sup>1,26</sup>, C. Sengupta<sup>1,27</sup>, K. Spekkens,<sup>28</sup> L. Staveley-Smith<sup>1,2,3</sup> and B. P. Wakker<sup>29</sup>

*Affiliations are listed at the end of the paper*

Accepted 2021 August 2. Received 2021 August 2; in original form 2021 June 11

## ABSTRACT

We present the Australian Square Kilometre Array Pathfinder (ASKAP) WALLABY pre-pilot observations of two ‘dark’ HI sources (with HI masses of a few times  $10^8 M_{\odot}$  and no known stellar counterpart) that reside within 363 kpc of NGC 1395, the most massive early-type galaxy in the Eridanus group of galaxies. We investigate whether these ‘dark’ HI sources have resulted from past tidal interactions or whether they are an extreme class of low surface brightness galaxies. Our results suggest that both scenarios are possible, and not mutually exclusive. The two ‘dark’ HI sources are compact, reside in relative isolation, and are more than 159 kpc away from their nearest HI-rich galaxy neighbour. Regardless of origin, the HI sizes and masses of both ‘dark’ HI sources are consistent with the HI size–mass relationship that is found in nearby low-mass galaxies, supporting the possibility that these HI sources are an extreme class of low surface brightness galaxies. We identified three analogues of candidate primordial ‘dark’ HI galaxies within the TNG100 cosmological, hydrodynamic simulation. All three model analogues are dark matter dominated, have assembled most of their mass 12–13 Gyr ago, and have not experienced much evolution until cluster infall 1–2 Gyr ago. Our WALLABY pre-pilot science results suggest that the upcoming large-area HI surveys will have a significant impact on our understanding of low surface brightness galaxies and the physical processes that shape them.

**Key words:** surveys – galaxies: evolution – galaxies: formation – galaxies: ISM.

## 1 INTRODUCTION

Previous HI large-area surveys have revealed ‘dark galaxies’ or HI-dominated systems with no optical counterparts to be very rare (Kilborn et al. 2000; Ryder et al. 2001; Kilborn et al. 2006; Haynes, Giovanelli & Kent 2007; Wong et al. 2009; Giovanelli et al. 2010; Adams, Giovanelli & Haynes 2013; Oosterloo, Heald & de Blok 2013; Serra et al. 2015b; Madrid et al. 2018; Lee-Waddell et al. 2019). These HI-dominated systems are often remnants of past tidal (or hydrodynamic) interactions and/or could be more extreme cousins of very low surface brightness galaxies such as the class of HI-rich tidal dwarf galaxies (Bournaud et al. 2007; Lelli et al. 2015; Lee-Waddell et al. 2016; Leisman et al. 2016; Sengupta et al. 2017) and ‘almost-dark’ galaxies (e.g. Leisman et al. 2017; Janowiecki et al. 2019; Sengupta et al. 2019; Scott et al. 2021). Galaxy evolution models have demonstrated that the majority of HI clouds without optical counterparts are likely the result of galaxy–galaxy interactions (e.g. Bekki, Koribalski & Kilborn 2005; Duc & Bournaud 2008; Taylor et al. 2017) and have evolved from tidal streams. Currently, large extended HI streams are also relatively

rare and are typically discovered in galaxy groups and clusters in the nearby Universe (e.g. Schneider et al. 1983; Oosterloo & van Gorkom 2005; Haynes et al. 2007; Serra et al. 2013; Lee-Waddell et al. 2014). Recently, the discovery of HI tidal tails near NGC 1316 (also known as Fornax A) further constrained the favoured merger formation scenario for NGC 1316 that was previously proposed (Iodice et al. 2017; Serra et al. 2019). This suggests that our understanding of the typical early-type galaxy (ETG) formation scenario may improve if HI tails are found to be more common.

While star formation is relatively well understood in massive disc galaxies, the process of star formation in low surface brightness galaxies (and at its most extreme, ‘almost-dark’ or HI-rich ultra-diffuse galaxies) is still an area of active research (Roychowdhury et al. 2009, 2011, 2015; Hunter et al. 2011; Elmegreen & Hunter 2015). Using the Australian Square Kilometre Pathfinder (ASKAP; Johnston et al. 2007; Hotan et al. 2021), next-generation HI all-sky surveys such as the Widefield ASKAP L-band Legacy All-sky Blind survey (WALLABY; Koribalski et al. 2020) will enable astronomers to further understand the formation and evolutionary processes at play in this extreme class of sources.

Taking advantage of the large ASKAP field of view, WALLABY early-science observations investigated galaxy interactions in galaxy groups as well as the impact of the galaxy group environment on the

\* E-mail: ivy.wong@csiro.au (OIW); adam.stevens@uwa.edu.au (ARHS); biqing.for@uwa.edu.au (B-QF)

**Table 1.** Properties of the Eridanus group.

Property	Measurement	Reference <sup>a</sup>
Right ascension (J2000)	03:38:32.0	1
Declination (J2000)	−22:18:51.0	1
Distance	21.0 Mpc	1, 2
Velocity	$1657 \pm 4 \text{ km s}^{-1}$	1
Virial mass	$2.1 \pm 2.7 \times 10^{13} M_{\odot}$	1
Maximal radial extent	0.8 Mpc	1
$L_{\text{Xray}}(0.1\text{--}2.0 \text{ keV})$	$6.8 \times 10^{40} \text{ ergs s}^{-1}$	3

<sup>a</sup>Reference key: 1 – Brough et al. (2006); 2 – For et al. (2021); 3 – Omar & Dwarakanath (2005).

gas content and star formation of individual group galaxies (Serra et al. 2015b; Elagali et al. 2019; For et al. 2019; Kleiner et al. 2019; Lee-Waddell et al. 2019; Reynolds et al. 2019). Prior to the start of the ASKAP pilot survey period, the ASKAP WALLABY team obtained test observations of the Eridanus (NGC 1395) group (or subcluster) of galaxies. NGC 1395, the most massive ETG in the Eridanus group, has shell-like stellar structures, indicative of mergers and accretion events in the past several Gyr (Malin & Carter 1980; Quinn 1984). Stellar population analyses of the NGC 1395 globular clusters provide evidence for the active accretion of low-mass satellites (Escudero et al. 2018).

The Eridanus group (or subcluster) is part of the Eridanus ‘supergroup’, which is composed of three groups of galaxies that will eventually merge into a single cluster with a total mass of approximately  $7 \times 10^{13} M_{\odot}$  (Brough et al. 2006). The northern NGC 1407 subcluster is the most evolved subcluster with a significant X-ray halo – into which the Eridanus group (to the South of NGC 1407) is currently infalling (Willmer et al. 1989; Osmond & Ponman 2004; Omar & Dwarakanath 2005; Brough et al. 2006). The third subcluster, the NGC 1332 galaxy group (south-west of NGC 1407 and west of the Eridanus group), is the least evolved group with the largest fraction of spirals and irregular galaxies. To distinguish between the Eridanus supergroup/cluster and the NGC 1395 group (which is also known as the Eridanus group in previous publications), we refer to the NGC 1395 subcluster as the Eridanus group in this paper.

The Eridanus group was targeted by the WALLABY team in order to investigate the processes that occur in galaxies that reside in an in-falling subcluster. Such processes contribute towards the ‘pre-processing’ of galaxies, with the quenching of star formation in approximately a third of cluster galaxies estimated to be attributable to ‘pre-processing’ (e.g. Jung et al. 2018). Further details of these ASKAP pre-pilot test observations can be found in For et al. (2021). A summary of the properties of the Eridanus group can be found in Table 1. Throughout this paper we adopt the distance of 21 Mpc for the Eridanus group following For et al. (2021).

In this paper, we investigate the properties of two optically dark H I sources located within 363 kpc in projection of NGC 1395. These ‘dark’ H I sources, BW 033910-2223 (WALLABY J033911-222322, hereafter known as C1) and BW 033732-2359 (WALLABY J033723-235753, hereafter known as C2), have H I velocities within  $250 \text{ km s}^{-1}$  of the central velocity ( $1638 \text{ km s}^{-1}$ ; Table 1) of the NGC 1395 group. Both C1 and C2 were previously detected in the Basketweave survey (BW) using the 64-m Parkes radio telescope (Waugh 2005). However, only C2 was correctly identified to be an H I source without an optical counterpart. C1 was previously cross-matched with the optical galaxy, NGC 1403 (Doyle et al. 2005; Waugh 2005). Additional follow-up synthesis observations were made by Waugh (2005) using the Australia Telescope Compact

Array (ATCA) in order to obtain more accurate positions of the H I sources found from the Basketweave single-dish observations.

The identification of optical counterparts to C1 and C2 is hindered by the projected chance alignment between both C1 with a background galaxy (NGC 1403), and C2 with a foreground Galactic star. To determine the connection between C1 and NGC 1403, we obtained new optical spectroscopy of NGC 1403 to verify its recessional velocity that was measured more than a decade ago (e.g. Davies et al. 1987). While large galaxy clusters are known to have velocity dispersions that are greater than  $1000 \text{ km s}^{-1}$ , this is not expected for less massive galaxy groups such as the Eridanus group.

We describe our new observations and data processing in Section 2. Section 3 presents the optically dark H I clouds that we find within 363 kpc of NGC 1395. We present the ASKAP H I properties of C1 and C2 in Section 3.1. Using deep optical imaging from the Dark Energy Camera Legacy Survey Data Release 9 (Dey et al. 2019), we investigate the presence of optical (stellar) counterparts to C1 and C2 in Section 3.2. Section 4 investigates the origin and formation history of these H I clouds. A summary of our results is presented in Section 5. For consistency with the parent catalogue (For et al. 2021), we adopt a  $\Lambda$  Cold Dark Matter ( $\Lambda$ CDM) cosmology where  $\Omega_M = 0.27$ ,  $\Omega_{\Lambda} = 0.73$  and  $H_0 = 73 \text{ km s}^{-1} \text{ Mpc}^{-1}$ . We note that the results of this paper are not sensitive to the assumed cosmology as the Eridanus group is part of the Local Universe.

## 2 DATA

### 2.1 ASKAP observations

Towards the end of the official ASKAP Early Science period (when 31 antennae are correlated together across a bandwidth of 288 MHz) and before the commencement of the official ASKAP pilot surveys, we obtained pre-pilot test observations of the Eridanus group region (see Fig. 1). These test observations were conducted on behalf of the WALLABY survey (Koribalski et al. 2020). As the Eridanus group is extended in the north–south direction, we optimize the coverage of this region through two interleaving diamond-shaped footprints whereby the standard  $6 \times 6$  square footprint of 36 beams (Elagali et al. 2019; For et al. 2019; Kleiner et al. 2019; Lee-Waddell et al. 2019; Reynolds et al. 2019) is rotated by 45 deg. The standard calibrator, PKS 1934-638, is used to calibrate the gains and bandpass in these observations. See Table 2 for more details of these observations.

### 2.2 ASKAP data processing and verification

Following For et al. (2021) and Murugesan et al. (2021), the data in this paper is based on the ASKAP correlations with baselines shorter than 2 km. Due to the significant levels of radio frequency interference (RFI) in the lower 144 MHz of the 288 MHz bandpass, only the high-frequency half of the band of observations was calibrated and imaged using the ASKAPSOFT pipeline (Whiting et al. 2017).<sup>1</sup> The image cubes are produced using the Robust +0.5 weighting and are tapered so as to obtain a synthesized beam of  $30 \text{ arcsec} \times 30 \text{ arcsec}$ . The phase and leakage corrections are made using the sky model, phase self-calibration method. The continuum subtraction is conducted in two steps: first in the visibility plane, then in the final image plane before applying the necessary primary

<sup>1</sup><http://www.atnf.csiro.au/computing/software/askapsoft/sdp/docs/current/index.html>

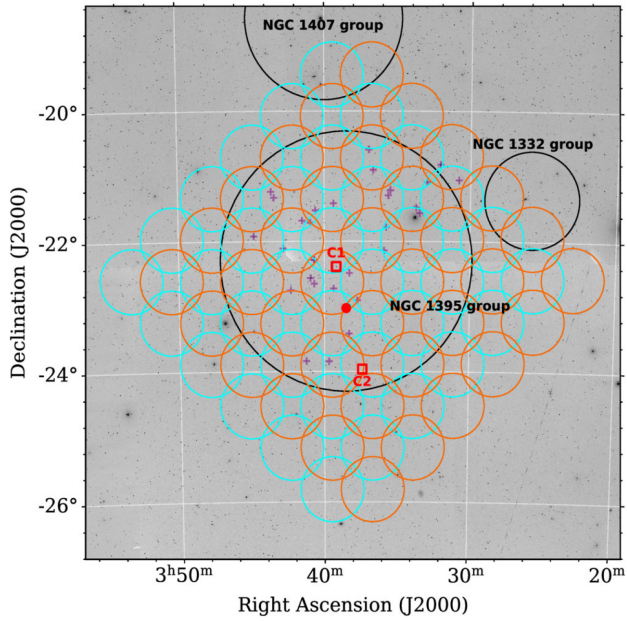


**Figure 1.** The diamond-shaped region mapped by Footprint A (cyan) and Footprint B (orange) of the Eridanus Cluster using ASKAP, overlaid on an optical map from the Digitized Sky Survey. Each footprint consists of 36 digitally formed beams. The black circles mark the maximum radial extents of the three galaxy groups that make up the Eridanus Cluster (Brough et al. 2006). The red dot marks the position of NGC 1395, the largest elliptical galaxy of the Eridanus group. The red squares mark the location of the two H I clouds (C1 and C2) with no obvious optical counterparts that are the subject of this paper. The purple crosses mark the location of galaxies that belong to the Eridanus group (Brough et al. 2006). The coordinates and recessional velocity of these galaxies can be found in Appendix A.

**Table 2.** Summary of the ASKAP observations on 2019 March 13.

Footprint	Centre (J2000)	SBID	Integration (hours)	Bandwidth (MHz)
(1)	(2)	(3)	(4)	(5)
A	03:39:30.0, −22:38:00	8168	5.8	288
B	03:36:44.5, −22:37:55	8170	5.0	288

*Notes.* Column (1): footprint ID; column (2): central right ascension and declination of footprint (J2000); column (3): ASKAP scheduling block ID; column (4): integration time in hours; column (5): instantaneous bandwidth of observations.

beam corrections. The final image cubes for each footprint are then mosaicked together in the image plane, beam by beam, to form the final 72-beam two-footprint observations of the Eridanus group. The default 18.5 kHz spectral resolution of the final image cubes results in channel widths that are  $\sim 4 \text{ km s}^{-1}$  at the frequency relevant to H I in the Eridanus group. The calibrated imaging products resulting from these observations can be downloaded from the CSIRO ASKAP Science Data Archive (CASDA).

The H I sources were automatically identified using the SoFiA source finder (version 2.0.1; Serra et al. 2015a; Westmeier et al. 2021). We refer the reader to For et al. (2021) for the complete description of the H I source catalogue mapped by these ASKAP pre-pilot observations. We mark the location of the two ‘dark’ H I sources that are the focus of this paper as open squares in Fig. 1. The H I source north of NGC 1395 is WALLABY J033911–222322

(hereafter known as C1) and the H I source south of NGC 1395 is WALLABY J033723–235745 (hereafter known as C2).

Previous observations of the same region from the Parkes Basketweave survey (BW) and its Australia Telescope Compact Array (ATCA) follow-up survey (Waugh 2005) enable a detailed verification study of these ASKAP pre-pilot observations. The Parkes BW observations reached an RMS of  $7 \text{ mJy beam}^{-1}$ , and the follow-up ATCA observations had a median RMS of  $6.5 \text{ mJy}$  with a synthesized beam of approximately  $113 \text{ arcsec} \times 296 \text{ arcsec}$ . We refer the reader to For et al. (2021) for the complete description of this verification study and the data quality assessment of these pre-pilot observations. We find that the RMS values of these ASKAP pre-pilot observations vary across the field and range between 2.4 and  $4.4 \text{ mJy}$ . The central beams typically have lower RMS than the beams at the edge of the field.

Following For et al. (2021), we include the additional 20 per cent flux correction factor to the measured H I integrated fluxes ( $S_{\text{H I}}$ ) in this paper.

### 2.3 Optical spectroscopy

In addition to the ASKAP observations, we obtained low-resolution optical spectroscopy of NGC 1403 using the WiFeS instrument on the 2.3 m telescope at Siding Springs Observatory on 2020 November 30 through Directors Discretionary Time allocation. The purpose of these observations was to verify the recessional velocity of NGC 1403 that had been measured more than a decade ago (e.g. Davies et al. 1987; Paturel et al. 2002).

Using the B3000 grating and the RT560 beam splitter, we obtained a total on-source exposure time of 120 min, which involved three pairs of 40 min on-source exposures, followed by a 15-min offset sky exposure. Standard calibration exposures were also obtained in addition to a 15-min exposure of the standard star, GD71. The spectral resolution from the B3000 grating is approximately  $2.2 \text{ \AA}$  and spans the wavelength range of  $3600\text{--}5700 \text{ \AA}$  (Dopita et al. 2010). These observations were calibrated and processed using the PYWIFES reduction pipeline (Childress et al. 2014). The recessional velocity of the calibrated spectrum was estimated using MARZ by fitting to an ETG template (Hinton et al. 2016).

## 3 RESULTS

### 3.1 The H I properties of C1 and C2

Our ASKAP position and velocity centres are flux-weighted centroids estimated by SoFiA. Table 3 presents the H I properties of C1 and C2 as parametrized by the SoFiA source finder (version 2.0.1; Serra et al. 2015a; Westmeier et al. 2021), in addition to H I properties measured by previous single-dish (Parkes Basketweave) and synthesis (ATCA) observations. Relative to the Basketweave detections, these new ASKAP observations find positional offsets of 37 arcsec and 2.6 arcmin for C1 and C2, respectively. Such positional offsets are unsurprising since we are comparing between Parkes observations with a 15.5 arcmin beam and ASKAP observations with a synthesized beam of 30 arcsec. In addition, ASKAP may resolve out the H I emission that exists on larger angular scales and consequently contribute towards an observed positional offset between the two sets of observations. When comparing between two sets of interferometric observations, we find smaller positional offsets between previous ATCA and ASKAP observations of 12 arcsec and 41 arcsec for C1 and C2. The velocity centres and linewidths of both C1 and C2 from the recent ASKAP observations are consistent with those found by the Parkes Basketweave survey and the ATCA

**Table 3.** Comparing the ASKAP observations of the two H I clouds to previous Basketweave single-dish (Parkes) and ATCA observations (Waugh 2005). The ASKAP H I recessional velocities follow the optical  $v = cz$  definition and the  $S_{\text{HI}}$  listed in this table includes the flux correction factor described by For et al. (2021).

Property (1)	Parkes (2)	ATCA (3)	ASKAP (this work) (4)
C1 properties			
RA	03:39:09.6	03:39:12.5	03:39:12
Dec	−22:23:47	−22:23:10	−22:23:22
$V_{50}$ (km s <sup>−1</sup> )	1876 ± 4	1879 ± 4	1879 ± 2
$W_{50}$ (km s <sup>−1</sup> )	41 ± 4	28 ± 2	23 ± 2
Beam	15.5 arcmin	113 arcsec × 297 arcsec	30 arcsec × 30 arcsec
RMS (mJy beam <sup>−1</sup> )	7.0	6.5	≈2.5
$S_{\text{HI}}$ (Jy km s <sup>−1</sup> )	3.0 ± 0.6	0.8	2.28 ± 0.18
$M_{\text{HI}}$ (M <sub>⊙</sub> )	3.1(±0.6) × 10 <sup>8</sup>	0.8 × 10 <sup>8</sup>	2.37(±0.19) × 10 <sup>8</sup>
$D_{\text{HI}}$ (kpc)	–	–	6.4 ± 1.1
C2 properties			
RA	03:37:31.7	03:37:24.7	03:37:23
Dec	−23:59:33	−23:58:25	−23:57:54
$V_{50}$ (km s <sup>−1</sup> )	1467 ± 7	1471 ± 3	1469 ± 2
$W_{50}$ (km s <sup>−1</sup> )	41 ± 7	17 ± 6	16 ± 2
Beam	15.5 arcmin	113 arcsec × 279 arcsec	30 arcsec × 30 arcsec
RMS (mJy beam <sup>−1</sup> )	7.0	6.5	2.4
$S_{\text{HI}}$ (Jy km s <sup>−1</sup> )	2.5 ± 0.6	0.9	1.35 ± 0.16
$M_{\text{HI}}$ (M <sub>⊙</sub> )	2.6(±0.6) × 10 <sup>8</sup>	0.9 × 10 <sup>8</sup>	1.41(±0.16) × 10 <sup>8</sup>
$D_{\text{HI}}$ (kpc)	–	–	7.0 ± 1.2

observations. Additionally, the ASKAP and ATCA velocity widths for C1 and C2 are in good agreement, but lower than the Basketweave values. Fig. 2 shows the H I moment zero maps of C1 and C2 overlaid as magenta contours over deep optical images, in addition to their H I spectra. The lowest column density contour displayed corresponds to the  $3\sigma$  column density level across the H I linewidth of each source.

Including the  $\sim 20$  per cent  $S_{\text{HI}}$  correction factor reported by For et al. (2021) for the ASKAP pre-pilot observations, we find that the ASKAP-derived  $S_{\text{HI}}$  for C1 is consistent with that found from the Parkes single-dish observations. On the other hand, the ASKAP observations detect only 54 per cent of  $S_{\text{HI}}$  that was found in C2 from Parkes (Waugh 2005). The significant H I flux deficit in the ASKAP measurements of C2 is consistent with, and likely related to the positional offset noted earlier, when comparing these ASKAP interferometric observations to Parkes single-dish observations.

The H I velocity widths listed in Table 3 and the spectra in Fig. 2 show that both C1 and C2 have narrow H I linewidths. Qualitatively, it is unclear from the H I velocity maps (Fig. 2) whether C1 and C2 are in stable rotation. To further investigate the possibility for rotating motions, we attempt to model the H I kinematics of C1 and C2. First we obtained a single Gaussian fit of the velocity field via a Bayesian Markov Chain Monte Carlo profile decomposition algorithm (BAYGAUD; Oh, Staveley-Smith & For 2019) which provided the input parameters into an automated two dimension (2D) Bayesian tilted-ring fitting tool, 2DBAT (Oh et al. 2018). We do not find evidence for a clear rotation pattern in C1. We are able to fit a rotating model to C2 using two 2DBAT set-ups. The first set-up had a constant position angle and inclination while fitting a cubic spline for the rotation velocity. In the second set-up, only the inclination was held constant and cubic splines are fitted for the rotation velocity and the position angle. Both set-ups resulted in rotating models with a maximum rotation velocity of  $\sim 35$  km s<sup>−1</sup>. We note that our results are significantly affected by beam smearing as C2 is only marginally resolved with only approximately two beams across its rotating axis.

In marginally resolved observations such as those for C2, it is more accurate to fit three dimensional (3D) kinematic models that take beam smearing effects into account, so we modelled the 3D kinematics of C2 using TiRiFiC (Józsa et al. 2007, 2021). We created two models for C2 where we assume that C2 is a finite-thickness disc with a flat rotation curve, a constant  $\text{sech}^2$  scale height and a constant velocity dispersion. One model assumed that we are observing C2 at a constant inclination of 90° (edge-on) and the second model allowed the inclination to vary (for a flat rotation curve) along with the surface brightness. For the edge-on model, we find a rotation amplitude of  $7.2 \pm 0.5$  km s<sup>−1</sup> and a velocity dispersion of  $8.1 \pm 0.3$  km s<sup>−1</sup>. For the second model, we find a rotation of  $22.7 \pm 5.7$  km s<sup>−1</sup> at an inclination of  $19.6 \pm 4.9$  deg and a velocity dispersion of  $8.4 \pm 0.2$  km s<sup>−1</sup>. It is clear from these 3D kinematic models that C2 is likely to be rotating and both models fit our observations equally well due to the low angular resolution of our ASKAP observations (see Fig. C1 in Appendix C). We note that it may also be possible for C2 to be rotating and observed face-on. However, we are not able to narrow down the inclinations and position angles of C2 (and consequently our models) from our ASKAP H I observations alone. Hence, our 3D kinematic models suggest that C2 is likely to have a true rotation velocity between  $7.2 \pm 0.5$  km s<sup>−1</sup> and  $22.7 \pm 5.7$  km s<sup>−1</sup>.

## 3.2 Optical search for stellar counterparts to C1 and C2

To investigate the presence of stellar components that could be associated with C1 and C2, we use the deep optical imaging from the publicly available Dark Energy Camera Legacy Survey Data Release 9 (DECaLS DR9; Dey et al. 2019). In addition to the improvement in surface brightness over previous data releases, DECaLS DR9 provides images where bright Galactic foreground stars have been modelled and subtracted. This is especially useful for our investigation of C2’s potential optical counterpart.

### 3.2.1 C1

The spectroscopic observations using the 2.3 m telescope at the Siding Springs Observatory (described in Section 2.3) find that NGC 1403 has a recessional velocity of  $4173 (\pm 135)$  km s<sup>−1</sup> – confirming that C1 is a foreground object that is associated with the Eridanus group, and not NGC 1403 as previously identified (Table 3). This recent measurement confirms previous spectroscopic observations and is consistent with results from peculiar velocity modelling by Cosmicflows-3 (Tully, Courtois & Sorce 2016; Tully et al. 2019; Pomarède et al. 2020). Velocity and density field reconstructions from Cosmicflows-3 find that C1 and the rest of the Eridanus group are travelling towards the Great Attractor; while NGC 1403 resides in a weak filament in the Sculptor void and is moving towards the Perseus-Pisces cluster. Fig. B1 in Appendix B illustrates the density field and velocity vectors of C1 (marked with a ‘1’) and NGC 1403 (marked with a ‘2’) determined by Cosmicflows-3.

At the location of C1, additional processing of the DECaLS DR9 images enables us to reach a surface brightness limit of  $\mu_{\text{lim},g} = 29.4$  mag arcsec<sup>−2</sup> and  $\mu_{\text{lim},r} = 29.1$  mag arcsec<sup>−2</sup> in the  $g$  and  $r$  bands, respectively. A detailed description for the method used to estimate the surface brightness limit can be found in appendix A of Román, Trujillo & Montes (2020). As C1 is projected in front of NGC 1403, we aim to differentiate between the optical component of NGC 1403 and any optical component associated with C1 by subtracting a simple model of NGC 1403 from the DR9 image.

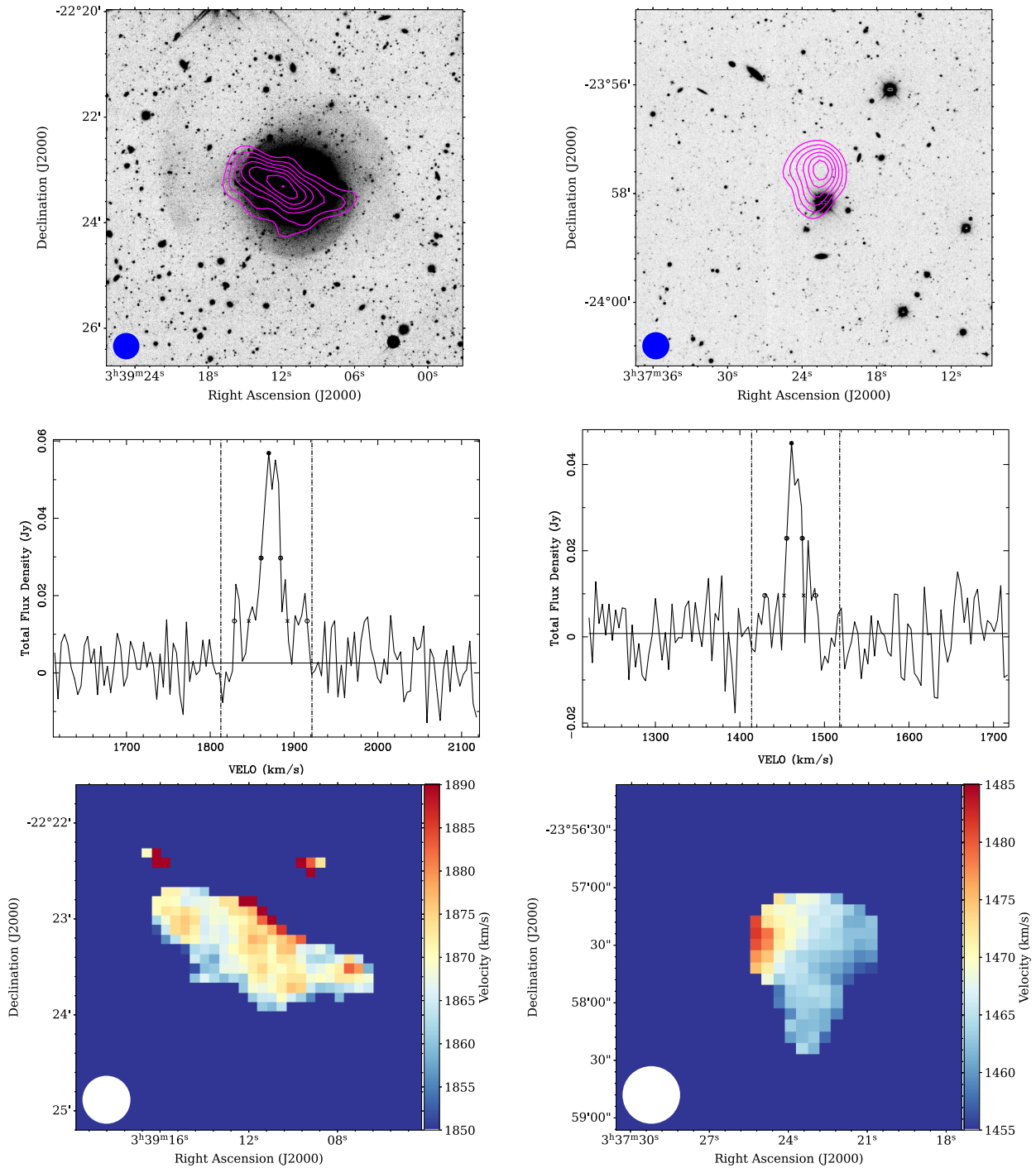


**Figure 2.** Top row: Moment zero H I column density maps of C1 (left column) and C2 (right column) overlaid on a deep optical image stack from DR8 and DR9 of the DECam Legacy Survey (Dey et al. 2019). Stellar shells from the background ETG behind C1 is shown by the deep DR9 imaging stack. We overlaid C2’s H I contours on to the DR8 optical image in order to show the location of the intervening foreground star. This foreground star has been subtracted in the DR9 optical images. The lowest H I contour levels for C1 and C2 begins at  $1.1 \times 10^{20}$  atoms  $\text{cm}^{-2}$  and subsequent contour levels are at increments of  $0.5 \times 10^{20}$  atoms  $\text{cm}^{-2}$ . The blue circle in the bottom-left of each panel in the top row represents the 30-arcsecond ASKAP synthesized beam. The middle row shows the H I spectra of both C1 (left) and C2 (right). The vertical lines mark the maximum velocity width of the H I profiles. The bottom row shows the 3 arcmin  $\times$  3 arcmin moment 1 maps of both C1 (left) and C2 (right). The H I emission below the H I column density of  $1.1 \times 10^{20}$  atoms  $\text{cm}^{-2}$  has been masked from these moment one maps.

While NGC 1403 is an ETG with a complex set of stellar shells, we assume that the central stellar body of NGC 1403 is consistent with a stellar density profile that is described by a Sersic model with an index of  $n = 4$ .

The deep optical imaging from DECaLS DR9 reveal a set of complex stellar shells that are affiliated with NGC 1403 (Fig. 3a). Fig. 3(b) shows the residual optical image of NGC 1403 after the subtraction of our simple ETG model. To further enhance

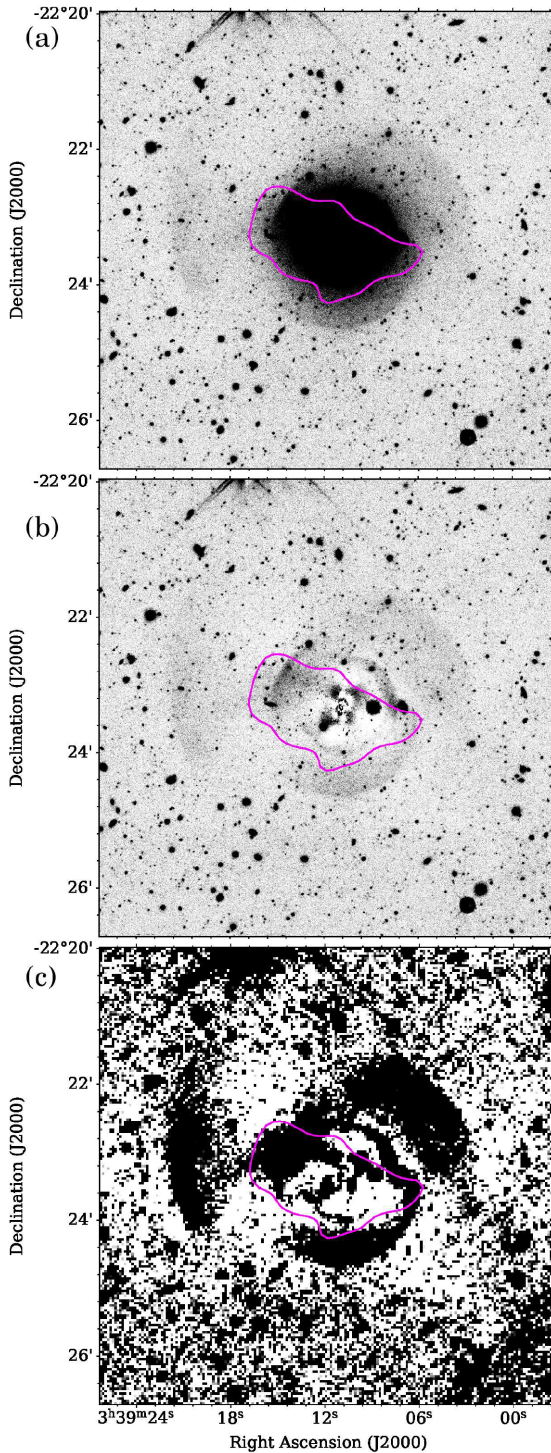


**Figure 3.** DECaLS DR9 *g*-band optical images of C1. The lowest column density H I moment zero contour at  $1.1 \times 10^{20} \text{ cm}^{-2}$  is shown as a magenta contour. Panels (a) and (b) show the optical images of NGC 1403 before and after an early-type galaxy model is subtracted, respectively. Panel (c) is a rebinned residual image where the residual image (panel b) is rebinned to a coarser pixel resolution to further enhance the surface brightness limit. All stellar structure correlate to NGC 1403’s large stellar shell complexes and a distinct stellar component from an additional low surface brightness galaxy is absent.

the signal-to-noise of any diffuse low surface brightness structures remaining in Fig. 3(b), we rebinned Fig. 3(b) to a coarser pixel scale (Fig. 3c). Figs 3(b) and (c) show that the diffuse stellar components are connected and not independent of NGC 1403’s stellar shells. Therefore we do not observe any distinct stellar component that could be associated with C1 and distinguishable from NGC 1403’s stellar structures. For greater context, the surface brightness limit attained from our DR9 images is approximately  $3 \text{ mag arcsec}^{-2}$  deeper than the SDSS data used in the identification of the optical counterparts for the H I-rich ultradiffuse galaxies by Leisman et al. (2017), ensuring that similarly low surface brightness objects can be detected in our optical images.

### 3.2.2 C2

Similar to C1, we investigate the presence of a stellar counterpart to C2 using the deep optical observations from DECaLS DR9 where the bright foreground star that is coincident with C2’s position has been modelled and subtracted. The top panel in Fig. 4 shows the DECaLS DR8 *g*-band image before the intervening foreground star is subtracted. The bottom panel of Fig. 4 shows the DECaLS DR9 *g*-band image where the star has been subtracted. The image has been rebinned to a coarser pixel resolution to further enhance the surface brightness sensitivity. The dominant emission appears to have arisen from the residuals of the stellar subtraction. We do not find a low surface brightness component that could be related to C2.

## 4 DISCUSSION: H I DEBRIS FROM PAST INTERACTIONS OR DARK GALAXY CANDIDATES?

In this section, we investigate the possible origin and nature of these two H I sources. Specifically, we explore the possibility that: (1) C1 and C2 originated from tidal interaction(s); and (2) C1 and C2 are primordial dark (or almost-dark) galaxies through investigating potential analogues from cosmological simulations. We conclude this section by comparing the H I properties of C1 and C2 to other classes of H I-dark (and low surface brightness) objects. We also discuss the implications of our results.

### 4.1 Investigating a tidal origin

The two optically dark WALLABY H I sources flanking the massive ETG, NGC 1395, may have originated from past galaxy interactions. Examples of H I tidal remnants through galaxy group interactions have been reported in previous ASKAP WALLABY early-science observations (e.g. Serra et al. 2015b; Lee-Waddell et al. 2019) as well as MeerKAT observations (e.g. Namumba et al. 2021).

A recent study of Fornax A (NGC 1316), another nearby ETG with comparable properties (stellar mass, shells, accretion history) to NGC 1395 suggested that H I streams extending 70–150 kpc away from the galaxy can result from multiple 10:1 merger events (Schweizer 1980; Iodice et al. 2017; Serra et al. 2019). The projected separations between C1 with NGC 1395 and C2 with NGC 1395 are at 238 and 363 kpc, respectively – beyond the 135 kpc radius of NGC 1395’s X-ray halo as well as its stellar shells (Brough et al. 2006; Tal et al. 2009; Escudero et al. 2018). Following the results of Kravtsov (2013), we estimate NGC 1395’s  $r_{200}$  (the radius at the density which is 200 times that of the critical density of the Universe) to be approximately 354 kpc assuming an optical effective radius of 48 arcsec (Lauberts & Valentijn 1989). At these projected distances

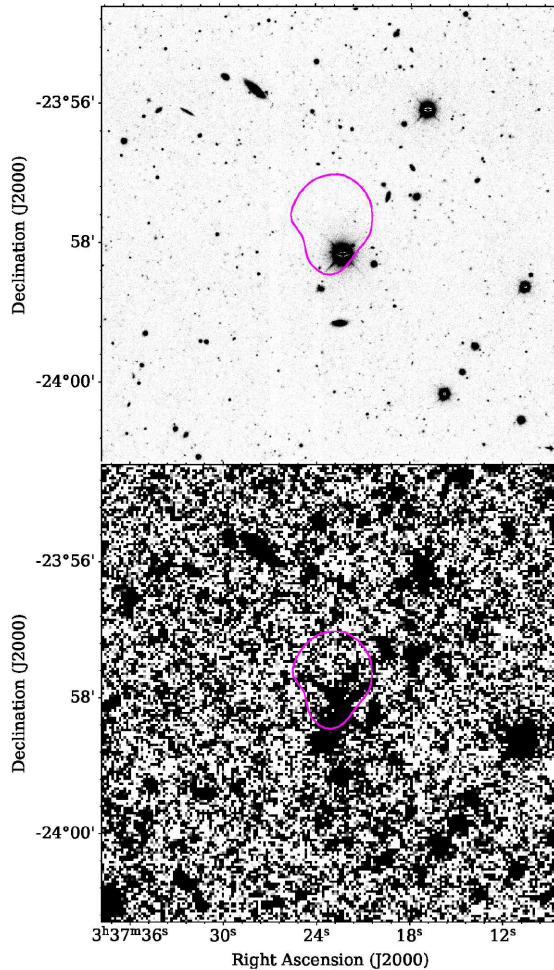


**Figure 4.** DECaLS DR8 and DR9  $g$ -band optical images of C2. The lowest column density H I moment zero contour at  $1.1 \times 10^{20} \text{ cm}^{-2}$  is shown as a magenta contour. The top panel shows the DECaLS DR8 image before the subtraction of the foreground star. The bottom panel shows the DR9 image where the foreground star has been subtracted and the entire image has been rebinned to a coarser resolution to further enhance the surface brightness of any faint stellar feature. The main structure observed in the bottom panel relates to residuals from the incomplete removal of the foreground star and no additional stellar structure is discernable that could be related to C2.

from NGC 1395, both C1 and C2 are not consistent with the projected distance of 15 effective radii that are typically observed in optically selected samples of tidal dwarf galaxies (TDGs; Kaviraj et al. 2012), which can be classed as almost-dark galaxies due to their low stellar surface brightnesses. These younger and less-evolved TDGs are still embedded within the tidal debris of their parent galaxies (e.g. Lelli et al. 2015). On the other hand, older and more evolved TDGs could be located further way from their parent galaxies (Bournaud & Duc 2006). Hence, we are not able to rule out the possibility that C1 and C2 are more evolved TDGs, from the projected separations alone. Regardless of projected separations, the young diffuse stellar populations within a TDG will likely fade into an almost-dark or dark galaxy within 2 Gyr, due to the aging of the stellar population (Román et al. 2021).

To differentiate between the possibility that C1 and C2 are candidate tidal remnants as opposed to candidate TDGs, we can compare our observed  $W_{50}$  for C1 and C2, to the simple expectation of circular velocity ( $v_G$ ) from a self-gravitating gas cloud via

**Table 4.** Tidal indices ( $\Theta$ ) determined between C1 and its nearest massive neighbours.

Neighbour (1)	$\log M_*$ ( $M_\odot$ ) (2)	Projected distance (kpc) (3)	$\Theta$ ( $\log_{10} [M_\odot \text{ Mpc}^{-3}]$ ) (4)
NGC 1395	10.9	238	1.8
NGC 1401	10.3	127	2.0
NGC 1415	10.3	163	1.7
ESO 482-G031	10.1	159	1.5

**Table 5.** Tidal indices ( $\Theta$ ) determined between C2 and its nearest massive neighbours.

Neighbour (1)	$\log M_*$ ( $M_\odot$ ) (2)	Projected distance (kpc) (3)	$\Theta$ ( $\log_{10} [M_\odot \text{ Mpc}^{-3}]$ ) (4)
NGC 1395	10.9	363	1.2
NGC 1385	10.0	197	1.2
ESO 482-G018	10.3	219	1.3
LSBG F482-037	10.1	90	2.3

$v_G = \sqrt{G \times 1.33 M_{\text{HI}} / R_{\text{HI}}}$  where  $G$  is the gravitational constant,  $M_{\text{HI}}$  and  $R_{\text{HI}}$  are the H I mass and H I radius, respectively. A factor of 1.33 is included to account for the contribution of Helium. We estimate  $v_G$  to be 20.6 and 15.2 km s $^{-1}$  for C1 and C2, respectively. Even though we only recover 54 per cent of the integrated H I flux of C2, the  $v_G$  values estimated for both C1 and C2 under the assumption of self-gravity are consistent with the observed  $W_{50}$  (Table 3). This comparison suggests that C1 and C2 are consistent with the circular velocities of simple self-gravitating systems, thereby favouring the hypothesis that C1 and C2 are TDG candidates over that of tidal remnants.

To further constrain the potential for more local interactions, we examine the nearest neighbouring galaxies to both C1 and C2. While the estimation of  $r_{200}$  for massive neighbouring galaxies is useful for constraining the possibility for gravitational interactions occurring between two galaxies, it is less useful for higher galaxy density environments where the halo potential is complicated by overlapping  $r_{200}$  from individual subhaloes. This is indeed the case for C1. Therefore, we use a tidal index,  $\Theta$  (Karachentsev, Makarov & Kaisina 2013; Pearson et al. 2016), to quantify the tidal influence between a neighbouring massive galaxy ( $M_* > 10^{10} M_\odot$ ) relative to C1 and C2. Following Pearson et al. (2016),  $\Theta$  is defined to be

$$\Theta = \log_{10} \left[ \frac{M_*}{10^{11} M_\odot} \left( \frac{D_{\text{proj}}}{\text{Mpc}} \right)^{-3} \right], \quad (1)$$

where  $M_*$  is the stellar mass and  $D_{\text{proj}}$  is the projected distance between C1 (or C2) and their nearest massive galaxy neighbour. Following Pearson et al. (2016), isolated environments are defined by  $\Theta < 0$ , intermediate and high density environments are traced by  $0 < \Theta < 1.5$  and  $\Theta > 1.5$ , respectively.

The nearest massive galaxies (where  $\log M_* \geq 10.0 M_\odot$ ) to C1 and C2 (in projection) are NGC 1401 and LSBG F482-037, respectively. Tables 4 and 5 list the tidal indices determined for C1 and C2 with respect to their nearest projected massive neighbours. Fig. 5 shows the galaxies neighbouring both C1 and C2. We find that  $\Theta = 2.0$  for C1 and NGC 1401. Using the stellar mass measured by For et al. (2021) for LSBG F482-037 of  $1.26 \times 10^{10} M_\odot$ , we find that  $\Theta = 2.3$  for C2. These tidal indices suggest that C1 and C2 may be under high tidal influence. However, the lack of H I in both NGC 1401 and



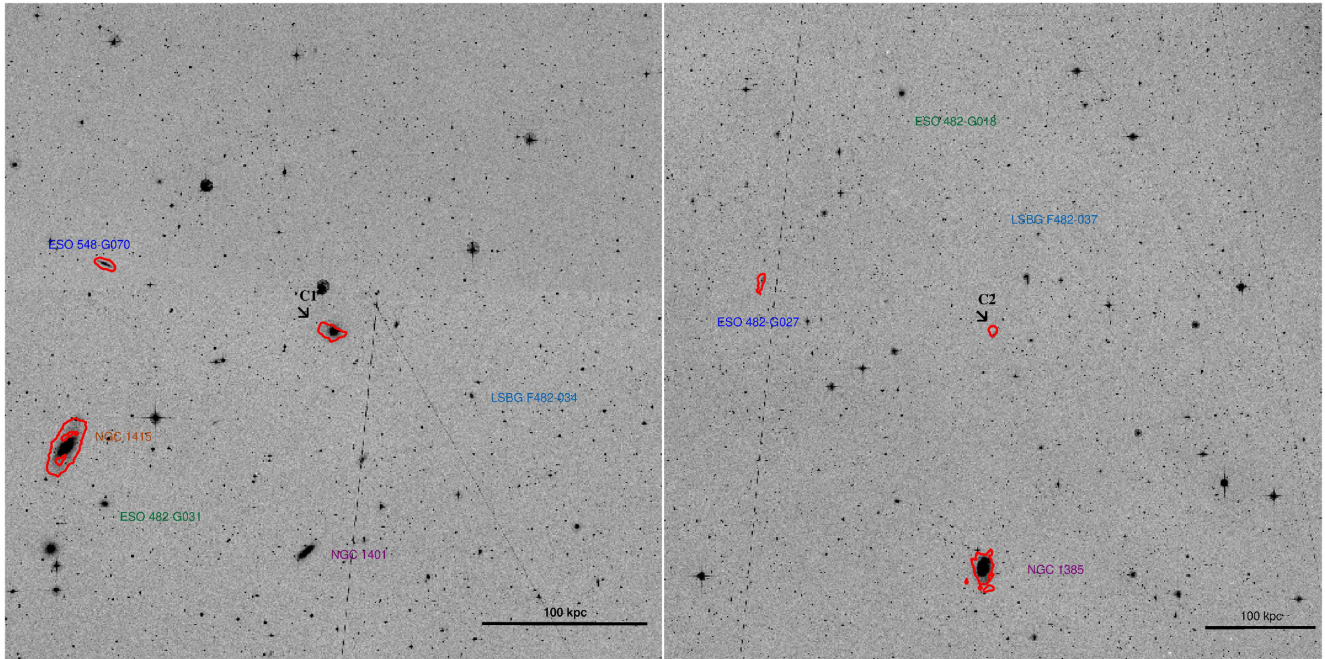


**Figure 5.** Map of C1 and C2, showing their nearest projected galaxy neighbours within  $500 \text{ km s}^{-1}$ . The WALLABY H I moment zero emission at the level of  $1.1 \times 10^{20} \text{ cm}^{-2}$  is outlined by the red contour, overlaid on a DSS blue background image centred on each of the dark WALLABY H I sources. A physical scale bar is provided in the bottom right corner of each panel. It should be noted that galaxies that are unlabelled reside in a more distant galaxy group at greater recessional velocities than C1 and C2. Also, the grey dashed line should be ignored as it is an artefact. Left panel: a  $1^\circ \times 1^\circ$  map centred on C1. Right panel: a  $1.5^\circ \times 1.5^\circ$  map centred on C2. North and east are to the top and left of the page, respectively.

LSBG F482-037 suggests that C1 and C2 are less likely to originate from NGC 1401 and LSBG F482-037, respectively.

The nearest massive galaxies to C1 and C2 (in projection) for which H I is detected are ESO 548-G070 and NGC 1385, respectively. Located at larger projected distances, the resulting  $\Theta$  values suggest that C1 and C2 may be under intermediate strength tidal influence. Since the tidal indices are only an approximate tracer of the tidal fields within which C1 and C2 reside, we cannot rule out the possibility that C1 and C2 have had a tidal origin. This is especially the case for C2 where our ASKAP observations appear to be missing 46 per cent of the total integrated H I that was measured from the Parkes Basketweave survey (Waugh 2005). Deeper H I observations will likely recover the true extent and further constrain the origin of C2.

The H I spectra of NGC 1415 and ESO 548-G070 are at lower recessional velocities than C1 (see Fig. 6), and we do not observe any signatures within the H I morphology or H I kinematics that would suggest any recent interactions. While we cannot completely rule out any interaction between all three H I sources in this field, the lack of any H I tail or extended structure does not provide strong support for interactions between the sources. The ASKAP H I centre position of C1 and H I mass are similar to that found from the Basketweave survey. The H I observations of C1 also do not appear to indicate that the H I is rotating. Follow-up observations with higher spectral resolution may provide further constraints on the kinematics and possibly the origin of C1.

C2 resides in a region south-west of NGC 1395 with four neighbouring galaxies. C2 is 32.4 arcmin ( $\approx 214 \text{ kpc}$  in projection) north of NGC 1385 (the closest H I-rich neighbour). While we do not find any H I emission extending between NGC 1385 and C2, both sources have consistent recessional velocities (see Fig. 7). Also,

the H I morphology of C2 and the lack of H I in LSBG F482-037 suggests that if C2 was a product of a past interaction, it is more likely to have originated from NGC 1385. This idea is supported by the fact that Parkes observations of C2 found the H I position centre to be 2.6 arcmin south-east of the ASKAP position centre and that the total H I emission from previous single-dish observations is nearly a factor of two greater than that observed by ASKAP. Hence, deeper follow-up H I observations may reveal more diffuse H I emission that could extend southwards towards NGC 1385.

In summary, the tidal indices estimated for both C1 and C2 suggest that we cannot rule out the tidal influences of local galaxy neighbours, and hence a possible tidal origin for these clouds. Despite the higher tidal indices estimated between C1 and C2 relative to their closest projected massive galaxy neighbours, we argue that H I from these closest projected neighbours are unlikely to be origins of both C1 and C2 due to the lack of H I in both nearest neighbours. The tidal indices estimated for C1 and C2 relative to their closest projected H I-rich neighbours suggest an intermediate-level of tidal influence. As the ASKAP H I observations of C1 fully recover the total integrated H I previously found from the Basketweave survey, C1 is a good candidate for an evolved TDG. Similarly, the observed H I velocity widths of C1 and C2 are also consistent with the approximate circular velocities of self-gravitating gas clouds, which suggests that C1 and C2 are more likely to be TDG candidates than young tidal remnants. As we do not observe any tidal tails in C2 at the measured  $3\sigma$  column density sensitivity of  $1.1 \times 10^{20} \text{ cm}^{-2}$ , future analysis of C2 would benefit from the feathering of single-dish observations with these ASKAP synthesis observations in order to probe the larger scale diffuse emission at lower column densities. Such future work would allow us to study the H I emission and structure at both arcsecond and arcminute scales.

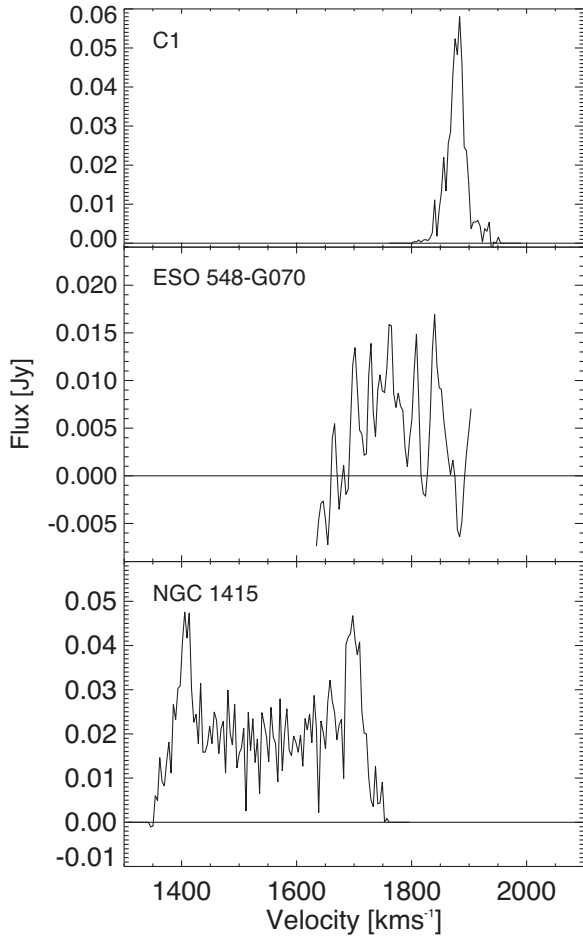


**Figure 6.** A comparison of C1’s H I spectrum (top panel) to that of its neighbouring H I-rich galaxies identified by SOFIA. It should be noted that ESO 548-G070 and NGC 1415 have WALLABY source names, WALLABY J034040–221711 and WALLABY J03406–223350 (For et al. 2021).

#### 4.2 Investigating a primordial origin

To explore the possible evolutionary history of C1 and C2 as primordial dark galaxy candidates (DGCs), we searched for sources with similar properties to C1 and C2 in the TNG100 cosmological simulations. The difference between DGCs discussed in this section and that of the almost-dark TDGs from the previous subsection is that the DGCs in this subsection formed in the early Universe, and not from tidal interactions in the last few billion years. Also, the primordial DGCs discussed in this section reside in their own dark matter halo prior to entry into the cluster or group environment at later times.

The TNG simulations were conducted with AREPO (Springel 2010), and follow  $\Lambda$ CDM with cosmological parameters from the Planck Collaboration ( $\Omega_m = 0.3089$ ,  $\Omega_b = 0.0486$ ,  $h = 0.6774$ ,  $\sigma_8 = 0.8159$ ; Planck Collaboration 2016). Prescriptions that describe the physical processes of baryons, including below the resolution limit, accounting for gas cooling, star formation, growth of massive black holes, magnetic fields and feedback from both stars and active galactic nuclei can be found in Weinberger et al. (2017) and Pillepich et al. (2018). TNG100 has a box length of  $75/h \simeq 110$  Mpc and a baryonic mass resolution of  $\sim 1.4 \times 10^6 M_\odot$ . Gas cells were post-processed to compute their atomic- and molecular- Hydrogen masses

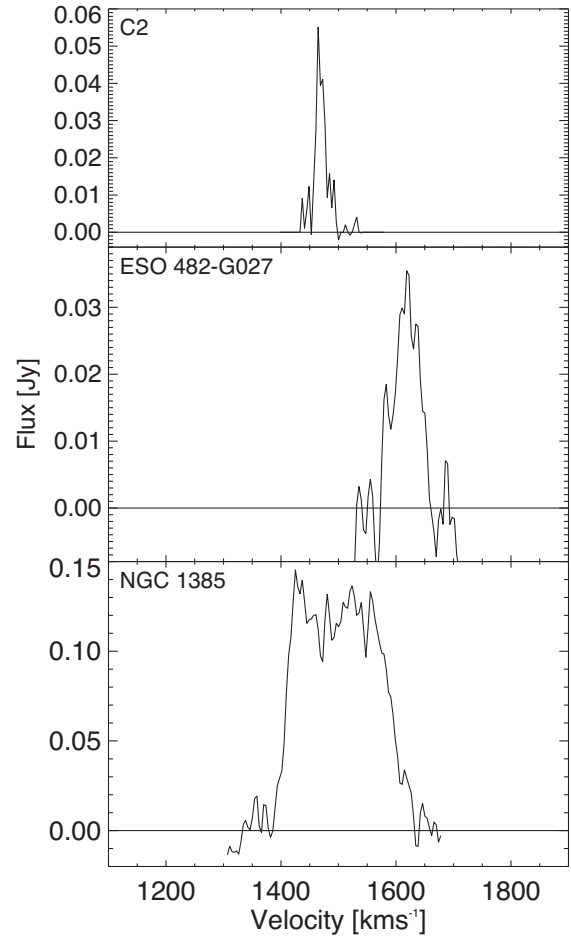


**Figure 7.** A comparison of C2’s H I spectrum (top panel) to that of its neighbouring H I-rich galaxies identified by SOFIA. It should be noted that ESO 482-G027 and NGC 1385 have WALLABY source names, WALLABY J033941–235054 and WALLABY J033728–243010 (For et al. 2021).

(Diemer et al. 2018; Stevens et al. 2019a). We use the following criteria for selecting analogue DGCs for C1 and C2 in TNG100:

- (i) satellite galaxies with stellar masses below  $10^{7.5} M_\odot$ . By TNG100 definition, such a stellar mass limit does imply an optically dark galaxy.
- (ii) H I masses between  $10^{8.0} - 10^{8.5} M_\odot$
- (iii) subhalo dark matter fractions above 5 per cent (to avoid numerical artefacts)
- (iv) host haloes of mass  $10^{13} \leq M_{200}/M_\odot \leq 10^{14.5}$ , whose central galaxies have neutral gas-to-stellar fractions that are less than 0.01. This halo mass range is consistent with that of the Eridanus group as well as the total halo mass of the eventual merger of all three subclusters within the Eridanus Cluster as per Brough et al. (2006).

We find three DGCs following this set of criteria. The three DGCs in TNG100 (hereafter known as TNG-DGC) reside within host haloes with  $\log_{10}(M_{200}/M_\odot) = 14.33, 13.80, \text{ and } 13.19$ . All three TNG-DGC (hereafter labelled by their subhalo IDs in the TNG public data base – 14081, 246257 and 88856) have dark matter fractions ranging from 97 to 98 per cent.

Fig. 8 presents the evolution history for each of the three TNG-DGCs. The top row of Fig. 8 shows the local environment in which each TNG-DGC resides at  $z = 0$  within a projected distance of

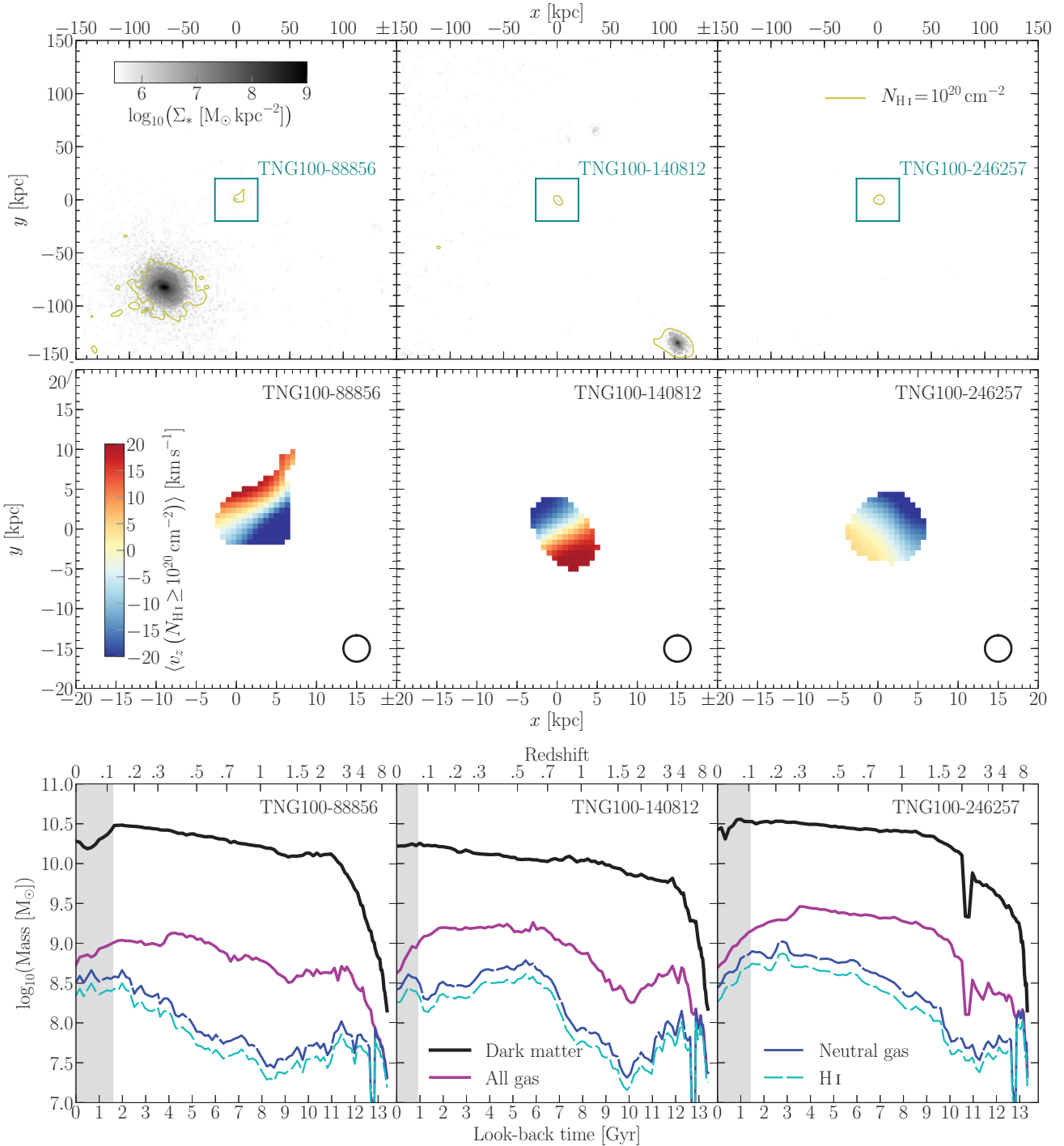


**Figure 8.** Images and evolutionary history of the three TNG-DGC (shown individually in three columns). Top row of panels: Images of each TNG-DGC and their immediate surroundings at  $z = 0$ . Greyscale is used to indicate stellar surface density, including any material within the host halo of the DGC (integrated along the line of sight). Contours show an H I column density of  $10^{20}$  atoms  $\text{cm}^{-2}$ . The  $(x, y) = (0, 0)$  position refers to the DGC’s centre of potential, as given in the TNG public data base (Nelson et al. 2019). Middle row of panels: H I-mass-weighted mean-velocity (moment 1) maps in the line of sight ( $z$ -direction) of each TNG-DGC. A minimum H I column density of  $10^{20}$  atoms  $\text{cm}^{-2}$  is imposed for the maps, where only gas bound to the TNG SUBFIND subhalo of interest is considered. The boundary of each panel matches the teal square in the top row of panels. For the purposes of visualization, we have approximated each gas cell as a sphere (subsequently collapsed into two dimensions), maintaining the cell’s actual volume in the simulation (see the `build_gas_image_array()` function at <https://github.com/arhstevens/Dirty-AstroPy/blob/master/galprops/galplot.py>). The circle in the bottom right corner of each panel represents the FWHM of the Gaussian kernel (FWHM = 3.3 kpc) with which the sources were convolved, in order for these models to be consistent with the observed WALLABY resolution. Bottom row of panels: Mass growth history of the TNG-DGCs. Each DGC is tracked back through the TNG SUBLINK merger trees (Rodríguez-Gomez et al. 2015), where all mass associated with the relevant SUBFIND subhalo at each snapshot is summed. ‘All gas’ means exactly that: ionized, neutral, hydrogen, and all other chemical species summed. ‘Neutral gas’ accounts for all atomic and molecular chemical species. The grey shaded region mark when each TNG-DGC became a satellite. To account for the reduced information available in TNG ‘mini snapshots’, we follow appendix B of Stevens et al. (2021) to calculate the neutral and H I mass at each snapshot for these panels.

**Table 6.** Dark matter (DM) and H I properties of the TNG-DGCs.

Property (1)	T100-88856 (2)	T100-140812 (3)	T100-246257 (4)
H I W50 (km s <sup>-1</sup> )	65.2	65.3	41.0
H I radius (kpc)	4.1	3.7	5.0
H I mass (M <sub>⊙</sub> )	1.0 × 10 <sup>8</sup>	1.1 × 10 <sup>8</sup>	1.3 × 10 <sup>8</sup>
DM mass (M <sub>⊙</sub> )	2.0 × 10 <sup>10</sup>	1.8 × 10 <sup>10</sup>	2.8 × 10 <sup>10</sup>

~150 kpc. The middle row of Fig. 8 shows the Moment 1 (H I-mass-weighted mean-velocity) maps for each TNG-DGC projected along the line of sight. While our ASKAP H I observations do not show clear rotation in C1 or C2, the TNG-DGC kinematics very clearly show rotating bulk motion. The bottom row of Fig. 8 shows the mass growth history of the TNG-DGCs. Assuming that the three TNG-DGC are bona fide analogues of C1 and C2, we can infer that C1 and C2 would also have built up most of their dark matter mass within the first 2 Gyr of formation and remained in a relatively uneventful evolutionary history. We note that the H I masses derived from TNG used three independent prescriptions (Gnedin & Kravtsov 2011; Krumholz 2013; Gnedin & Draine 2014) yielded results which are consistent (with each other) for all three TNG-DGCs.

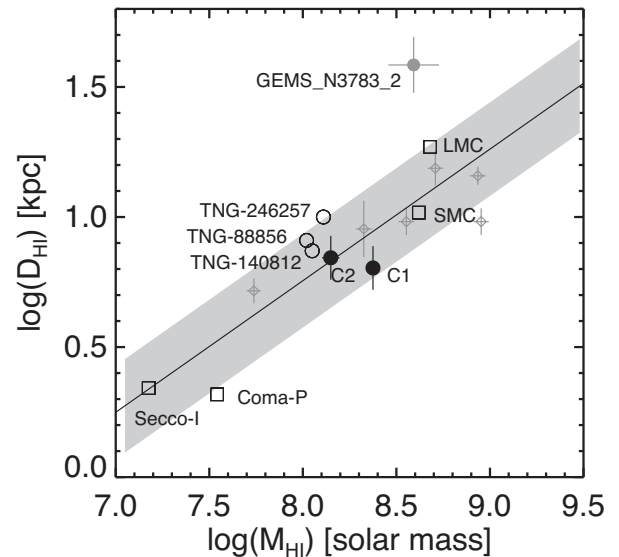
These TNG-DGCs suggest that H I-rich, DGCs within clusters could have formed at early times and remained dark due to a fairly uneventful evolutionary history whereby the cluster in-fall (in the past 1–2 Gyr) has only affected its total gas mass but that gas losses have not significantly impacted the star formation rate (SFR) of each of these galaxies. Hence, such DGCs will likely remain dark unless they are on orbital trajectories that lead to stronger interactions with other galaxies or their local environment.

Table 6 lists the H I properties of the three TNG-DGCs. We emphasize that the H I properties provided are not mock ASKAP properties but are TNG model properties. The three TNG-DGCs have properties close to the stellar mass and halo mass resolution limit of TNG100 but with sufficient particle resolution for a statistically accurate determination of global galaxy properties. A distinct difference between the three TNG-DGCs compared to C1 and C2 is that the TNG-DGCs are clearly rotating and have greater H I velocity widths (W50; Table 6), likely due to its significant dark matter fraction. On the one hand, the TNG-DGCs’ greater H I velocity widths could be due to the TNG-DGCs having had more time to build up their angular momentum, relative to that of C1 and C2. This is consistent with the suggestion that disc galaxies with high spins would be Toomre stable against star formation (Jimenez & Heavens 2020).

On the other hand, the greater H I velocity widths of the TNG-DGCs may be associated with the larger sizes (angular extents) that are typically found in TNG galaxies (see Section 4.3), a systematic feature of the TNG100 simulations that has been previously studied in Stevens et al. (2019b). As such, we are not able to conclude with absolute certainty that C1 and C2 have a primordial origin even though the TNG-DGCs are the closest model analogues from TNG100 to C1 and C2.

### 4.3 Comparison to other known low surface brightness objects

In addition to the H I fluxes and moment maps, our new ASKAP H I observations are at sufficient surface brightness sensitivity and angular resolution that we are able to compare both C1 and C2’s H I sizes and H I masses to other known ‘dark’ (and almost-dark) low surface brightness sources. Such a comparison may provide further insights towards our understanding of such a class of sources that



**Figure 9.** The two dark H I sources (C1 and C2; solid black circle) are consistent with the H I size–mass relationship of low-mass galaxies in the Local Universe (solid line and grey-shaded 3 $\sigma$  scatter) from Wang et al. (2016). The H I size–mass properties of the Small and Large Magellanic Clouds (Staveley-Smith et al. 1998, 2003), Secco-I (Sand et al. 2017) and Coma-P (Brunker et al. 2019) are shown as open squares for comparison purposes. The TNG-DGCs are represented by black open circles and the rotationally supported TDGs from Lelli et al. (2015) are shown as small grey open diamonds. The previously discovered optically dark H I-rich source GEMS\_N3783.2 (Kilborn et al. 2006) is represented by a large grey solid circle.

while currently rare, are increasing in numbers as the next-generation H I surveys get underway. We determine the H I diameters ( $D_{\text{HI}}$ ) of C1 and C2 out to a gas surface density of 1 M<sub>⊙</sub> pc<sup>-2</sup> to be 6.4 kpc and 7.0 kpc, respectively (Table 3).

The H I size–mass relationship is typically observed in rotationally supported galaxies, and has been attributed to the small range of H I gas densities within galaxies (Wang et al. 2016; Stevens et al. 2019b). Fig. 9 compares the H I sizes and masses of C1 and C2 to the TNG-DGCs described in the previous subsection, as well as other low surface brightness, almost-dark low-mass galaxies such as the Magellanic Clouds, Secco-I and Coma-P (Brunker et al. 2019), a sample of rotating TDGs from Lelli et al. (2015), as well as a previously reported optically dark H I source (GEMS\_N3783.2) that resides in the NGC 3783 galaxy group (Kilborn et al. 2006). In general, the three TNG-DGCs have H I-sizes and masses that are consistent with the H I size–mass relationship from Wang et al. (2016). The TNG-DGCs have similar H I masses to C1 and C2 but larger diameters than those of C1 and C2.

Fig. 9 shows that both C1 and C2 are: (1) consistent with the H I size–mass relationship that is found for low-mass and low surface brightness galaxies in the Local Universe, including rotationally supported TDGs; (2) only a factor of a few less massive in H I than both the Small and Large Magellanic Clouds; and (3) factors of a few more massive than the ‘almost-dark’ galaxies, Coma-P (Brunker et al. 2019) or Secco-I (Sand et al. 2017). The consistency of C1’s and C2’s H I properties with that of the H I size–mass relationship may be suggestive of rotational support at some level even if our current ASKAP H I observations only show support for rotation in C2. On the other hand, the previously discovered H I-rich optically dark source, GEMS\_N3783.2 is less consistent with the H I size–

mass relationship. Perhaps GEMS\_N3783.2 is at an earlier stage of evolution? Previous active searches for H I-rich optically dark sources in Local Volume galaxy groups have also revealed dark massive H I sources to be very rare and concluded that these massive H I clouds are likely to originate from strong galaxy interactions (Chynoweth et al. 2011). From Fig. 9 alone, it appears that C1 and C2 have H I sizes and masses that are consistent with other rotating, low-mass galaxies whether or not C1 and C2 have a past tidal or primordial origin.

In terms of the stellar content, we are not able to identify any stellar component for either C1 or C2 (Section 3.2). Assuming that the observed rotation in C2 implies that C2 is stable and is consistent with a stable disc star formation model described by Wong et al. (2016), we could expect the SFR of C2 to range between 0.01 and 0.03  $M_{\odot} \text{ yr}^{-1}$ . For comparison, the more massive (than C1 and C2) Small Magellanic Cloud (SMC) has an SFR of 0.05  $M_{\odot} \text{ yr}^{-1}$  (e.g. Wilke et al. 2004). The stellar mass of the SMC is  $1.5 \times 10^9 M_{\odot}$  (Wilke et al. 2004) and has sufficient stellar surface brightness to be detectable at the distance of the Eridanus group. A simple back-of-the-envelope estimation suggests that C2 could build up approximately  $10^7 M_{\odot}$  of stars if it were able to sustain this SFR (of 0.01–0.03  $M_{\odot} \text{ yr}^{-1}$ ) for 1 Gyr or more. Even so, C2 is still more than two orders of magnitude less massive (and likely at lower stellar surface density) than the SMC. Furthermore, we know from Román et al. (2021) that the optical surface brightness will further diminish as the stellar population ages. Hence, it is unsurprising that we are not able to detect a significant stellar population within C2.

#### 4.4 Implications

The upcoming WALLABY survey provides an important step forward in the study of H I galaxy evolution as it overcomes the angular-resolution limitation from previous single-dish large-area H I surveys such as HIPASS (Barnes et al. 2001) and ALFALFA (Giovannelli et al. 2005), through synthesis imaging. On the other hand, interferometric observations trades angular resolution for surface brightness sensitivity. Furthermore, the intrinsic lack of zero-spacing information in the visibility ( $uv$ -) plane translates to a potential for ‘resolving out’ emission that exists on large angular scales. So far, WALLABY early-science commissioning and pilot observations have successfully recovered the total H I emission from a diverse set of H I observations of galaxies in environments ranging from the field to groups and clusters (Serra et al. 2015b; Elagali et al. 2019; For et al. 2019; Kleiner et al. 2019; Lee-Waddell et al. 2019; Reynolds et al. 2019; Wang et al. 2021)

The ASKAP pre-pilot observations presented in this paper targets a galaxy group that is in an active state of cluster infall, and galaxies within this group are understood to be experiencing active ‘pre-processing’ (For et al. 2021; Murugesan et al. 2021). Therefore, the probability of H I existing at a large range of densities and angular extents is higher than in non-interacting galaxies that reside in less dynamic environments. While our ASKAP synthesis observations did not fully recover the total integrated H I emission for C2 from previous Parkes observations, we note that we have recovered more H I emission than previous ATCA synthesis observations, even though the ATCA observations had a larger synthesized beam than ASKAP. This demonstrates the superior performance in *both* surface brightness sensitivity and angular resolution that we can expect from the upcoming WALLABY survey using ASKAP. On the other hand, deeper H I observations to better surface brightness sensitivities are required to map the full extent of diffuse tidal structures (e.g. Namumba et al. 2021).

The two dark H I sources reported in this paper are potential candidates for an extreme class of objects that would not have been found through targeted surveys of optically bright galaxies. While the H I kinematics of the TNG-DGC do not match those of C1 and C2, we are not able to completely rule out a primordial origin without more sensitive and higher resolution follow-up H I observations and modelling. We recover the same total integrated H I flux for C1 as previously measured from single-dish observations, but we only recover 54 per cent of the integrated H I flux for C2.

If both C1 and C2 have a tidal origin and are TDG candidates, then C1 and C2 may be at different stages of TDG evolution. Based on the complete recovery of the total H I emission of C1 and the agreement in position between our ASKAP observations and those from Parkes, we can argue for C1 to be at a more advanced stage of TDG evolution relative to that of C2. On the other hand, the observed rotation in C2’s H I emission does favour C2 to be at a more stable self-gravitating state than C1 where rotation is absent. The possibility also remains that both C1 and C2 to have originated through different formation and evolutionary processes. Such heterogeneity in formation pathways is consistent with recent findings that low surface brightness galaxies (or ultradiffuse galaxies) have multiple formation and evolutionary pathways (e.g. Yozin & Bekki 2015; Papastergis, Adams & Romanowsky 2017; Román & Trujillo 2017; Bennet et al. 2018; Ferré-Mateu et al. 2018; Janowiecki et al. 2019; Sales et al. 2020). As H I-rich low surface brightness galaxies represent a subset and possibly a younger demographic of the low surface brightness Universe, such samples are useful in the study of star formation at low densities and efficiencies — an area of active and current research (e.g. McGaugh, Schombert & Lelli 2017; Thilker et al. 2019).

Further analysis of C1 and C2, including the H I emission at larger angular scales, as well as more sophisticated methods for the identification of the possible stellar components will be required to verify whether these sources are remnants of past tidal interactions or bona fide extreme examples of almost-dark galaxies. We note that it is non-trivial to identify the stellar components of both C1 and C2 from deep optical or near-infrared imaging as there is a chance alignment along the line of sight of C1 and C2 with a background ETG and a foreground star, respectively.

## 5 CONCLUSIONS

We present new ASKAP WALLABY pre-pilot H I observations of two dark H I clouds projected within 363 kpc of NGC 1395 in the Eridanus group, WALLABY J033911-222322 (C1) and WALLABY J033723-235745 (C2). Previous association of C1 to NGC 1403 is incorrect, and no detectable stellar components could be attributed to C1 and C2. We are neither able to confirm that these sources have a tidal origin nor are primordial dark (or almost-dark) galaxies.

The relationship of C1 (and any possible interaction) with its H I-rich neighbours is not obvious. The ASKAP synthesis pre-pilot observations recover all of the H I emission found from previous Parkes single-dish observations, and the ASKAP position is consistent with the Parkes single-dish centroid to within the positional uncertainties of the Parkes observations. Our ASKAP pre-pilot observations recover only 54 per cent of C2’s integrated H I that was previously measured by the Parkes Basketweave survey. Furthermore the position offset between the ASKAP and Parkes observations is in the direction of NGC 1385, within whose  $r_{200}$  C2 is hypothesized to reside. In addition, the velocity of C2’s H I emission is the same as NGC 1385’s recessional velocity. Hence if both C1 and C2 have

a tidal origin and are candidate TDGs, then C1 is likely to be in a different stage of evolution than C2.

In the hypothetical situation that one or both dark H I sources are primordial dark galaxy candidates, we find from the TNG100 simulations that these sources likely formed in the early Universe more than 12 Gyr ago and had a relatively sedate evolutionary history whereby not much happened until the in-fall into a cluster environment 2 Gyr ago. However, the observed differences between the H I kinematics of C1 and C2, relative to those of the TNG-DGC suggests that more detailed modelling and more sensitive observations are required before any firmer conclusions can be made.

From a technical perspective, it is reassuring that these pre-pilot ASKAP synthesis observations have provided an improvement in terms of surface brightness sensitivity and angular resolution, relative to past observations with the ATCA and during the early science phase of observations with ASKAP. In this respect, the WALLABY survey will help further our understanding by providing a more complete census of the H I Universe, as well as the low surface brightness ‘dark’ Universe.

## ACKNOWLEDGEMENTS

We thank the anonymous referee for a constructive review of this paper. Parts of this research was supported by the Australian Research Council Centre of Excellence for All-sky Astrophysics in 3 Dimensions (ASTRO 3D) through project number CE170100013. OIW acknowledges discussions with Elaine Sadler which helped improved this manuscript. ARHS acknowledged receipt of the Jim Buckee Fellowship at ICRAR/UWA. SHO acknowledges support from the National Research Foundation of Korea (NRF) grant funded by the Korea government (Ministry of Science and ICT: MSIT) (No. NRF-2020R1A2C1008706). LVM and JR acknowledges financial support from the grants AYA2015-65973-C3-1-R and RTI2018-096228-B-C31 (MINECO/FEDER, UE), as well as from the State Agency for Research of the Spanish MCIU through the ‘Center of Excellence Severo Ochoa’ award to the Instituto de Astrofísica de Andalucía (SEV-2017-0709). JR acknowledges support from the State Research Agency (AEI-MCINN) of the Spanish Ministry of Science and Innovation under the grant ‘The structure and evolution of galaxies and their central regions’ with reference PID2019-105602GB-I00/10.13039/501100011033. FB acknowledges funding from the European Research Council (ERC) under the European Union’s Horizon 2020 - Research and Innovation Framework Programme (grant agreement No.726384/Empire). AB acknowledges support from the Centre National d’Etudes Spatiales (CNES), France. PK is partially supported by the BMBF project 05A17PC2 for D-MeerKAT. This work was supported by Fundação para a Ciência e a Tecnologia (FCT) through the research grants UIDB/04434/2020 and UIDP/04434/2020. TCS acknowledges support from FCT through national funds in the form of a work contract with the reference DL 57/2016/CP1364/CT0009.

The Australian SKA Pathfinder is part of the Australia Telescope National Facility which is managed by CSIRO. Operation of ASKAP is funded by the Australian Government with support from the National Collaborative Research Infrastructure Strategy. ASKAP uses the resources of the Pawsey Supercomputing Centre. Establishment of ASKAP, the Murchison Radio-astronomy Observatory, and the Pawsey Supercomputing Centre are initiatives of the Australian Government, with support from the Government of Western Australia and the Science and Industry Endowment Fund. We acknowledge the Wajarri Yamatji people as the traditional owners of the Observatory site.

This publication makes use of the NASA/IPAC Extragalactic Database (NED), which is operated by the Jet Propulsion Laboratory, California Institute of Technology, under contract with the National Aeronautics and Space Administration.

This project used public archival data from the Dark Energy Survey (DES). Funding for the DES Projects has been provided by the U.S. Department of Energy, the U.S. National Science Foundation, the Ministry of Science and Education of Spain, the Science and Technology Facilities Council of the United Kingdom, the Higher Education Funding Council for England, the National Center for Supercomputing Applications at the University of Illinois at Urbana-Champaign, the Kavli Institute of Cosmological Physics at the University of Chicago, the Center for Cosmology and Astro-Particle Physics at the Ohio State University, the Mitchell Institute for Fundamental Physics and Astronomy at Texas A&M University, Financiadora de Estudos e Projetos, Fundação Carlos Chagas Filho de Amparo à Pesquisa do Estado do Rio de Janeiro, Conselho Nacional de Desenvolvimento Científico e Tecnológico and the Ministério da Ciência, Tecnologia e Inovação, the Deutsche Forschungsgemeinschaft, and the Collaborating Institutions in the Dark Energy Survey. The Collaborating Institutions are Argonne National Laboratory, the University of California at Santa Cruz, the University of Cambridge, Centro de Investigaciones Energéticas, Medioambientales y Tecnológicas-Madrid, the University of Chicago, University College London, the DES-Brazil Consortium, the University of Edinburgh, the Eidgenössische Technische Hochschule (ETH) Zürich, Fermi National Accelerator Laboratory, the University of Illinois at Urbana-Champaign, the Institut de Ciències de l’Espai (IEEC/CSIC), the Institut de Física d’Altes Energies, Lawrence Berkeley National Laboratory, the Ludwig-Maximilians-Universität München and the associated Excellence Cluster Universe, the University of Michigan, the National Optical Astronomy Observatory, the University of Nottingham, the Ohio State University, the OzDES Membership Consortium, the University of Pennsylvania, the University of Portsmouth, SLAC National Accelerator Laboratory, Stanford University, the University of Sussex, and Texas A&M University. Based in part on observations at Cerro Tololo Inter-American Observatory, National Optical Astronomy Observatory, which is operated by the Association of Universities for Research in Astronomy (AURA) under a cooperative agreement with the National Science Foundation. Data base access and other data services are provided by the NOAO Data Lab.

## DATA AVAILABILITY

These pre-pilot observations are publicly available from the CSIRO ASKAP Science Data Archive (CASDA; Chapman 2015; Huynh et al. 2020). Specifically, the visibilities and H I data cubes for these observations can be found using this DOI: <https://dx.doi.org/10.25919/kqrt-pv24>

## REFERENCES

- Adams E. A. K., Giovanelli R., Haynes M. P., 2013, *ApJ*, 768, 77  
 Barnes D. G. et al., 2001, *MNRAS*, 322, 486  
 Bekki K., Koribalski B. S., Kilborn V. A., 2005, *MNRAS*, 363, L21  
 Bennet P., Sand D. J., Zaritsky D., Crnojević D., Spekkens K., Karunakaran A., 2018, *ApJ*, 866, L11  
 Bournaud F., Duc P. A., 2006, *A&A*, 456, 481  
 Bournaud F. et al., 2007, *Science*, 316, 1166  
 Brough S., Forbes D. A., Kilborn V. A., Couch W., Colless M., 2006, *MNRAS*, 369, 1351

- Brunker S. W. et al., 2019, *AJ*, 157, 76
- Chapman J. M., 2015, in IAU General Assembly. p. 2232458
- Childress M. J., Vogt F. P. A., Nielsen J., Sharp R. G., 2014, *Astrophys. Space Sci.*, 349, 617
- Chynoweth K. M., Holley-Bockelmann K., Polisensky E., Langston G. I., 2011, *AJ*, 142, 137
- Davies R. L., Burstein D., Dressler A., Faber S. M., Lynden-Bell D., Terlevich R. J., Wegner G., 1987, *ApJS*, 64, 581
- Dey A. et al., 2019, *AJ*, 157, 168
- Diemer B. et al., 2018, *ApJS*, 238, 33
- Dopita M. et al., 2010, *Astrophys. Space Sci.*, 327, 245
- Doyle M. T. et al., 2005, *MNRAS*, 361, 34
- Duc P.-A., Bournaud F., 2008, *ApJ*, 673, 787
- Elagali A. et al., 2019, *MNRAS*, 487, 2797
- Elmegreen B. G., Hunter D. A., 2015, *ApJ*, 805, 145
- Escudero C. G., Faifer F. R., Smith Castelli A. V., Forte J. C., Sesto L. r. A., González N. M., Scalia M. C., 2018, *MNRAS*, 474, 4302
- Ferré-Mateu A. et al., 2018, *MNRAS*, 479, 4891
- For B.-Q. et al., 2019, *MNRAS*, 489, 5723
- For B.-Q. et al., 2021, *MNRAS*, in press
- Giovanelli R. et al., 2005, *AJ*, 130, 2598
- Giovanelli R., Haynes M. P., Kent B. R., Adams E. A. K., 2010, *ApJ*, 708, L22
- Gnedin N. Y., Draine B. T., 2014, *ApJ*, 795, 37
- Gnedin N. Y., Kravtsov A. V., 2011, *ApJ*, 728, 88
- Haynes M. P., Giovanelli R., Kent B. R., 2007, *ApJ*, 665, L19
- Hinton S. R., Davis T. M., Lidman C., Glazebrook K., Lewis G. F., 2016, *Astron. Comput.*, 15, 61
- Hotan A. W. et al., 2021, *PASA*, 38, 9
- Hunter D. A., Elmegreen B. G., Oh S.-H., Anderson E., Nordgren T. E., Massey P., Wilsey N., Riabokin M., 2011, *AJ*, 142, 121
- Huynh M., Dempsey J., Whiting M. T., Ophel M., 2020, in Ballester P., Ibsen J., Solar M., Shorridge K., eds. ASP Conf. Ser. Vol. 522, Astronomical Data Analysis Software and Systems XXVII. Astron. Soc. Pac., San Francisco. p. 263
- Iodice E. et al., 2017, *ApJ*, 839, 21
- Janowiecki S., Jones M. G., Leisman L., Webb A., 2019, *MNRAS*, 490, 566
- Jimenez R., Heavens A. F., 2020, *MNRAS*, 498, L93
- Johnston S. et al., 2007, *PASA*, 24, 174
- Józsa G. I. G., Kenn F., Klein U., Oosterloo T. A., 2007, *A&A*, 468, 731
- Józsa G. I. G. et al., 2021, *MNRAS*, 501, 2704
- Jung S. L., Choi H., Wong O. I., Kimm T., Chung A., Yi S. K., 2018, *ApJ*, 865, 156
- Karachentsev I. D., Makarov D. I., Kaisina E. I., 2013, *AJ*, 145, 101
- Kaviraj S., Darg D., Lintott C., Schawinski K., Silk J., 2012, *MNRAS*, 419, 70
- Kilborn V. A. et al., 2000, *AJ*, 120, 1342
- Kilborn V. A., Forbes D. A., Koribalski B. S., Brough S., Kern K., 2006, *MNRAS*, 371, 739
- Kleiner D. et al., 2019, *MNRAS*, 488, 5352
- Koribalski B. S. et al., 2020, *Astrophys. Space Sci.*, 365, 118
- Kravtsov A. V., 2013, *ApJ*, 764, L31
- Krumholz M. R., 2013, *MNRAS*, 436, 2747
- Lauberts A., Valentijn E. A., 1989, The Surface Photometry Catalogue of the ESO-Uppsala Galaxies. European Southern Observatory, Garching
- Lee-Waddell K. et al., 2014, *MNRAS*, 443, 3601
- Lee-Waddell K. et al., 2016, *MNRAS*, 460, 2945
- Lee-Waddell K. et al., 2019, *MNRAS*, 487, 5248
- Leisman L., Haynes M. P., Giovanelli R., Józsa G., Adams E. A. K., Hess K. M., 2016, *MNRAS*, 463, 1692
- Leisman L. et al., 2017, *ApJ*, 842, 133
- Lelli F. et al., 2015, *A&A*, 584, A113
- McGaugh S. S., Schombert J. M., Lelli F., 2017, *ApJ*, 851, 22
- Madrid J. P., Lee-Waddell K., Serra P., Koribalski B. S., Schirmer M., Spekkens K., Wang J., 2018, *ApJ*, 854, L6
- Malin D. F., Carter D., 1980, *Nat*, 285, 643
- Murugesan C. et al., 2021, *MNRAS*, in press
- Namumba B. et al., 2021, *MNRAS*, 505, 3795
- Nelson D. et al., 2019, *Comput. Astrophys. Cosmol.*, 6, 2
- Oh S.-H., Staveley-Smith L., Spekkens K., Kamphuis P., Koribalski B. S., 2018, *MNRAS*, 473, 3256
- Oh S.-H., Staveley-Smith L., For B.-Q., 2019, *MNRAS*, 485, 5021
- Omar A., Dwarakanath K. S., 2005, *JA&A*, 26, 1
- Oosterloo T., van Gorkom J., 2005, *A&A*, 437, L19
- Oosterloo T. A., Heald G. H., de Blok W. J. G., 2013, *A&A*, 555, L7
- Osmond J. P. F., Ponman T. J., 2004, *MNRAS*, 350, 1511
- Papastergis E., Adams E. A. K., Romanowsky A. J., 2017, *A&A*, 601, L10
- Patuel G., Dubois P., Petit C., Woelfel F., 2002, LEDA
- Pearson S. et al., 2016, *MNRAS*, 459, 1827
- Pillepich A. et al., 2018, *MNRAS*, 473, 4077
- Planck Collaboration, 2016, *A&A*, 594, A13
- Pomarède D., Tully R. B., Graziani R., Courtois H. M., Hoffman Y., Lezmy J., 2020, *ApJ*, 897, 133
- Quinn P. J., 1984, *ApJ*, 279, 596
- Reynolds T. N. et al., 2019, *MNRAS*, 482, 3591
- Rodríguez-Gomez V. et al., 2015, *MNRAS*, 449, 49
- Román J., Trujillo I., 2017, *MNRAS*, 468, 4039
- Román J., Trujillo I., Montes M., 2020, *A&A*, 644, A42
- Román J., Jones M. G., Montes M., Verdes-Montenegro L., Garrido J., Sánchez S., 2021, *A&A*, 649, L14
- Roychowdhury S., Chengalur J. N., Begum A., Karachentsev I. D., 2009, *MNRAS*, 397, 1435
- Roychowdhury S., Chengalur J. N., Kaisin S. S., Begum A., Karachentsev I. D., 2011, *MNRAS*, 414, L55
- Roychowdhury S., Huang M.-L., Kauffmann G., Wang J., Chengalur J. N., 2015, *MNRAS*, 449, 3700
- Ryder S. D. et al., 2001, *ApJ*, 555, 232
- Sales L. V., Navarro J. F., Peñafiel L., Peng E. W., Lim S., Hernquist L., 2020, *MNRAS*, 494, 1848
- Sand D. J. et al., 2017, *ApJ*, 843, 134
- Schneider S. E., Helou G., Salpeter E. E., Terzian Y., 1983, *ApJ*, 273, L1
- Schweizer F., 1980, *ApJ*, 237, 303
- Scott T. C., Sengupta C., Lagos P., Chung A., Wong O. I., 2021, *MNRAS*, 503, 3953
- Sengupta C., Scott T. C., Paudel S., Dwarakanath K. S., Saikia D. J., Sohn B. W., 2017, *MNRAS*, 469, 3629
- Sengupta C., Scott T. C., Chung A., Wong O. I., 2019, *MNRAS*, 488, 3222
- Serra P. et al., 2013, *MNRAS*, 428, 370
- Serra P. et al., 2015a, *MNRAS*, 448, 1922
- Serra P. et al., 2015b, *MNRAS*, 452, 2680
- Serra P. et al., 2019, *A&A*, 628, A122
- Springel V., 2010, *MNRAS*, 401, 791
- Staveley-Smith L., Kim S., Putman M., Stanimirović S., 1998, *Rev. Mod. Astron.*, 11, 117
- Staveley-Smith L., Kim S., Calabretta M. R., Haynes R. F., Kesteven M. J., 2003, *MNRAS*, 339, 87
- Stevens A. R. H. et al., 2019a, *MNRAS*, 483, 5334
- Stevens A. R. H., Diemer B., Lagos C. d. P., Nelson D., Obreschkow D., Wang J., Marinacci F., 2019b, *MNRAS*, 490, 96
- Stevens A. R. H. et al., 2021, *MNRAS*, 502, 3158
- Tal T., van Dokkum P. G., Nelan J., Bezanson R., 2009, *AJ*, 138, 1417
- Taylor R., Davies J. I., Jáchym P., Keenan O., Minchin R. F., Palouš J., Smith R., Wünsch R., 2017, *MNRAS*, 467, 3648
- Thilker D. et al., 2019, *BAAS*, 51, 525
- Tully R. B., Courtois H. M., Sorce J. G., 2016, *AJ*, 152, 50
- Tully R. B., Pomarède D., Graziani R., Courtois H. M., Hoffman Y., Shaya E. J., 2019, *ApJ*, 880, 24
- Wang J., Koribalski B. S., Serra P., van der Hulst T., Roychowdhury S., Kamphuis P., Chengalur J. N., 2016, *MNRAS*, 460, 2143
- Wang J. et al., 2021, *ApJ*, 915, 70
- Waugh M., 2005, PhD thesis, University of Melbourne
- Weinberger R. et al., 2017, *MNRAS*, 465, 3291
- Westmeier T. et al., 2021, *MNRAS*, 506, 3962
- Whiting M., Voronkov M., Mitchell D., Askap Team, 2017, in Lorente N. P. F., Shorridge K., Wayth R., eds. ASP Conf. Ser. Vol. 512, Astronomical Data

Analysis Software and Systems XXV. Astron. Soc. Pac., San Francisco, p. 431  
 Wilke K., Klaas U., Lemke D., Mattila K., Stickel M., Haas M., 2004, *A&A*, 414, 69  
 Willmer C. N. A., Focardi P., da Costa L. N., Pellegrini P. S., 1989, *AJ*, 98, 1531  
 Wong O. I., Webster R. L., Kilborn V. A., Waugh M., Staveley-Smith L., 2009, *MNRAS*, 399, 2264

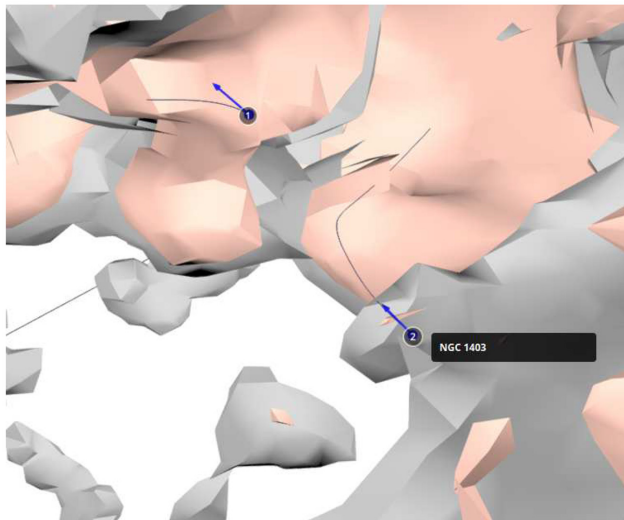
Wong O. I., Meurer G. R., Zheng Z., Heckman T. M., Thilker D. A., Zwaan M. A., 2016, *MNRAS*, 460, 1106  
 Yozin C., Bekki K., 2015, *MNRAS*, 452, 937

## APPENDIX A: GALAXY MEMBERS OF THE ERIDANUS GROUP

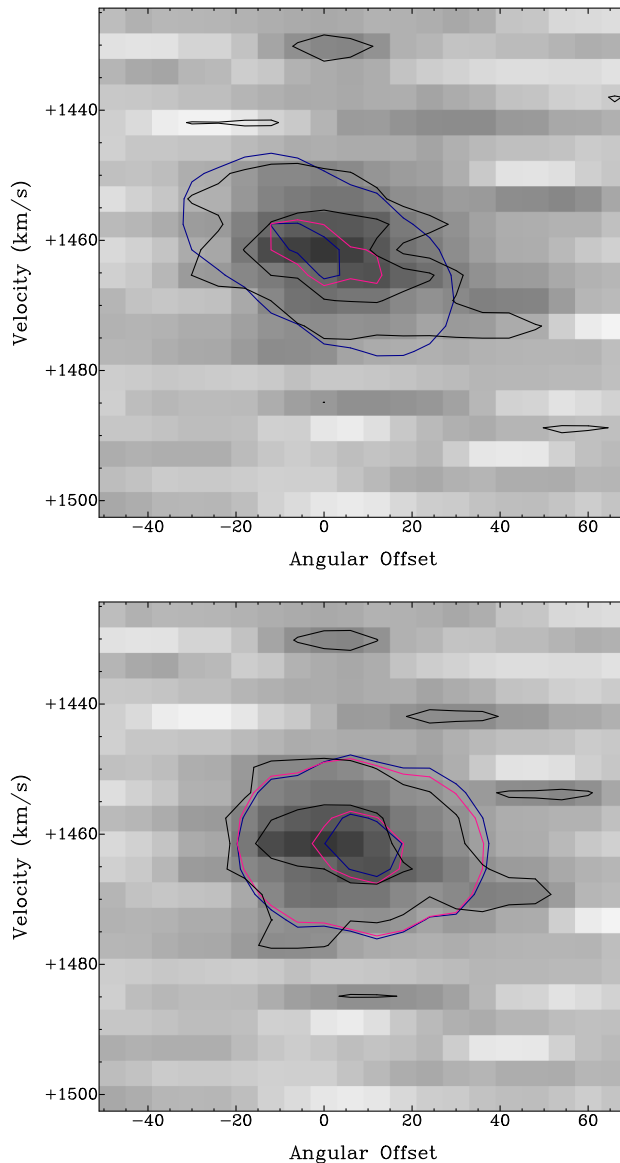
**Table A1.** Galaxy members of the Eridanus group as defined by Brough et al. (2006).

Galaxy	RA (J2000)	Dec (J2000)	$v$ (km s <sup>-1</sup> )
ESO 482–G 017	03:37:43.33	–22:54:29.5	1515
LSBG F482–034	03:38:16.55	–22:29:11.4	1359
2MASX J03355395–2208228	03:35:53.95	–22:08:23.0	1374
2MASX J03354520–2146578	03:35:45.27	–21:46:59.2	1638
ESO 548–G 036	03:33:27.69	–21:33:52.9	1520
ESO 548–G 034	03:32:57.63	–21:05:21.9	1707
NGC 1353	03:32:02.98	–20:49:08.2	1587
2MASX J03365674 – 2035231	03:36:56.75	–20:35:23.0	1689
NGC 1377	03:36:39.07	–20:54:07.2	1809
ESO 548–G 069	03:40:36.17	–21:31:32.4	1647
NGC 1414	03:40:57.14	–21:42:49.9	1752
APMUKS(BJ) B034114.27–212912	03:43:26.46	–21:19:44.2	1711
NGC 1422	03:41:31.07	–21:40:53.5	1680
NGC 1415	03:40:56.86	–22:33:52.1	1659
ESO 482–G 031	03:40:41.54	–22:39:04.1	1803
ESO 548–G 029	03:30:47.17	–21:03:29.6	1215
IC 1953	03:33:41.87	–21:28:43.1	1867
ESO 548–G 049	03:35:28.27	–21:13:02.2	1510
IC 1962	03:35:37.38	–21:17:36.8	1806
ESO 482–G 018	03:38:17.64	–23:25:09.0	1687
NGC 1395	03:38:29.72	–23:01:38.7	1717
MCG –04 – 09 –043	03:39:21.57	–21:24:54.6	1588
NGC 1401	03:39:21.85	–22:43:28.9	1495
ESO 482–G 035	03:41:14.65	–23:50:19.9	1890
NGC 1426	03:42:49.11	–22:06:30.1	1443
ESO 549–G 006	03:43:38.25	–21:14:13.7	1609
NGC 1439	03:44:49.95	–21:55:14.0	1670
APMUKS(BJ) B033830.70–222643	03:40:41.35	–22:17:10.5	1737
ESO 482–G 027	03:39:41.21	–23:50:39.8	1626
ESO 548–G 070	03:40:40.99	–22:17:13.4	1422
ESO 482–G 036	03:42:18.80	–22:45:09.2	1567



**APPENDIX B: COSMICFLOWS-3 DENSITY FIELD OF THE REGION BETWEEN C1 AND NGC 1403**


**Figure B1.** The reconstructed density of the region between C1 (marked ‘1’) and NGC 1403 (marked ‘2’) from Cosmicflows-3 (Tully et al. 2016). The blue vectors show the velocity trajectory of C1 towards the Great Attractor and NGC 1403 towards the Perseus-Pisces Supercluster.

**APPENDIX C: COMPARING THE 3D KINEMATIC MODELS FOR C2**


**Figure C1.** Position–velocity diagrams of C2 (black contour) along the major (top) and minor (bottom) axes of the modelled disc. The ‘flat’ model (where the inclination is allowed to vary) and the ‘edge-on’ model (where the inclination is fixed at  $90^\circ$ ) are represented by the blue and pink contours respectively. We find that both 3D kinematic models fit the observations equally well despite the inclination differences – a direct consequence of the low angular resolution of the observations.

- <sup>1</sup>ATNF, CSIRO, Space & Astronomy, PO Box 1130, Bentley, WA 6102, Australia
- <sup>2</sup>International Centre for Radio Astronomy Research, University of Western Australia, 35 Stirling Highway, Crawley, WA 6009, Australia
- <sup>3</sup>ARC Centre of Excellence for All-Sky Astrophysics in 3 Dimensions (ASTRO 3D), Australia
- <sup>4</sup>Centre for Astrophysics and Supercomputing, Swinburne University of Technology, Hawthorn, Victoria 3122, Australia
- <sup>5</sup>Department of Physics and Astronomy, Sejong University, 209 Neungdong-ro, Gwangjin-gu, Seoul 05006, Republic of Korea
- <sup>6</sup>South African Radio Astronomy Observatory, 2 Fir Street, Black River Park, Observatory, Cape Town 7925, South Africa
- <sup>7</sup>Department of Physics and Electronics, Rhodes University, PO Box 94, Makhanda 6140, South Africa
- <sup>8</sup>Argelander-Institut für Astronomie, Universität Bonn, Auf dem Hügel 71, D-53121 Bonn, Germany
- <sup>9</sup>Instituto de Astrofísica de Andalucía, CSIC, Glorieta de la Astronomía, E-18080 Granada, Spain
- <sup>10</sup>Instituto de Astrofísica de Canarias, c/ Vía Láctea s/n, E-38205 La Laguna, Tenerife, Spain
- <sup>11</sup>Departamento de Astrofísica, Universidad de La Laguna, E-38206 La Laguna, Tenerife, Spain
- <sup>12</sup>Univ Lyon, Univ Claude Bernard Lyon 1, IUF, IP2I Lyon, F-69622 Villeurbanne, France
- <sup>13</sup>Institut de Recherche sur les Lois Fondamentales de l'Univers, CEA Université Paris-Saclay, F-91191 Gif Sur Yvette, France
- <sup>14</sup>CSIRO, Space & Astronomy, PO Box 76, Epping, NSW 1710, Australia
- <sup>15</sup>Aix Marseille Univ, CNRS, CNES, LAM, F-13013 Marseille, France
- <sup>16</sup>ASTRON, The Netherlands Institute for Radio Astronomy, NL-7991 PD Dwingeloo, the Netherlands
- <sup>17</sup>Telethon Kids Institute, Perth Children's Hospital, Perth 6009, Australia
- <sup>18</sup>Department of Physics and Astronomy, University of Louisville, 102 Natural Science Building, Louisville, KY 40292, USA
- <sup>19</sup>Faculty of Physics and Astronomy, Astronomical Institute, Ruhr University Bochum, D-44780 Bochum, Germany
- <sup>20</sup>INAF - Osservatorio Astronomico di Cagliari, Via della Scienza 5, I-09047 Selargius (CA), Italy
- <sup>21</sup>School of Science, Western Sydney University, Locked Bag 1797, Penrith, NSW 2751, Australia
- <sup>22</sup>INAF - Arcetri Astrophysical Observatory, Largo Enrico Fermi 5, I-50125 Florence, Italy
- <sup>23</sup>Department of Physics and Astronomy, The University of Texas Rio Grande Valley, , Brownsville, TX 78520, USA
- <sup>24</sup>Department of Physics and Astronomy, Rutgers University, 136 Frelinghuysen Road, Piscataway, NJ 08854, USA
- <sup>25</sup>TMC Data Science, High Tech Campus 96, NL-5656 AG Eindhoven, the Netherlands
- <sup>26</sup>Institute of Astrophysics and Space Sciences (IA), Rua das Estrelas, P-4150-762 Porto, Portugal
- <sup>27</sup>Purple Mountain Observatory (CAS), No. 8 Yuanhua Road, Qixia District, Nanjing 210034, China
- <sup>28</sup>Department of Physics and Space Science, Royal Military College of Canada, PO Box 17000, Station Forces, Kingston, Ontario K7K 7B4, Canada
- <sup>29</sup>University of Wisconsin-Madison, 475 N Charter St, Madison, WI 53706, USA

This paper has been typeset from a  $\text{\TeX/L\AA\TeX}$  file prepared by the author.